

Research

**Phenomenological Studies on
Melt-Structure-Water Interactions (MSWI)
during Postulated Severe Accidents:
Year 2004 Activity**

APRI 5 Report

B.R. Sehgal
H.S. Park
A.K. Nayak
R.C. Hansson
D. Chiferaw
A. Stepanyan
R.S. Rao
A. Karbojian

April 2005

Forskningsprojektet APRI-5 är ett samarbetsprojekt mellan följande organisationer:

- Statens kärnkraftinspektion
- Ringhals AB
- OKG Aktiebolag
- Forsmarks Kraftgrupp AB
- Barsebäck Kraft AB

Projektet är underställd en styrgrupp med representanter från SKI och kraftbolagen enligt följande:

Mauritz Gärdinge, OKG (ordförande)

Oddbjörn Sandervåg, SKI

Ninos Garis, SKI

Anders Henoeh, Ringhals

Ingvar Berglund, FKA

Erik Larsen, BKAB

Lennart Agrenius, Agrenius Ingenjörbyrå (projektledare)

Research

Phenomenological Studies on Melt-Structure-Water Interactions (MSWI) during Postulated Severe Accidents: Year 2004 Activity

APRI 5 Report

B.R. Sehgal
H.S. Park
A.K. Nayak
R.C. Hansson
D. Chiferaw
A. Stepanyan
R.S. Rao
A. Karbojian

Division of Nuclear Power Safety
Department of Energy Technology
Royal Institute of Technology
SE_100 44 Stockholm
Sweden

April 2005

This report concerns a study which has been conducted for the Swedish Nuclear Power Inspectorate (SKI). The conclusions and viewpoints presented in the report are those of the author/authors and do not necessarily coincide with those of the SKI.

CONTENTS

SUMMARY	2
1 INTRODUCTION AND RESEARCH OBJECTIVES.....	3
2 PROGRESS OF RESEARCH PROGRAM.....	6
2.1 In-Vessel and Ex-Vessel Debris Coolability	6
2.1.1 POMEKO Program	6
2.1.1.1 Top Flooding	7
2.1.1.2 Effect of non-condensable gas injection on quenching.....	8
2.1.1.3 Top flooding with side water injection	8
2.1.1.4 Top and bottom flooding with the downcomers	9
2.1.2 COMEKO Program.....	13
2.1.3 SIMEKO Program.....	17
2.1.4 SIMEKO Experiment	17
2.1.4.1 Two-layer simulations.....	18
2.1.4.2 Three-layer simulations.....	18
2.1.4.3 Steady-state temperature distribution in the liquid pool.....	19
2.1.4.4 Heat flux distribution in the sidewall.....	20
2.1.4.5 Upward and downward heat fluxes	21
2.2 Ex-Vessel Steam Explosion.....	23
2.2.1 MISTEE Experimental Program	23
2.2.1.1 Metallic melt tests	23
2.2.1.2 Oxidic melt tests	26
2.2.1.3 Development of simultaneous visualization system	27
2.2.2 Steam Explosion Analysis with the COMETA Code	28
2.2.2.1 Simulation of the FARO L-33 Test	29
2.2.2.2 Simulation of TROI experiments.....	32
3 SUMMARY OF YEAR 2004 RESEARCH PROGRAM	35
4 RESEARCH PLAN OF YEAR 2005 RESEARCH PROGRAM	38
Reference (2004 Publication List).....	38

SUMMARY

This report presents descriptions of the major results obtained in the research program “Melt-Structure-Water Interaction (MSWI)” at NPS/KTH during the year 2004. The primary objectives of the MSWI Project in year 2004 were to study (1) the in-vessel and ex-vessel melt/debris bed coolability process when melt is flooded with water, and (2) the energetics and characteristics of steam explosions. Our general approaches are to establish scaling relationships so that the data obtained in the experiments could be extended to prototypical accident geometries and conditions, develop phenomenological or computational models for the processes under investigation and validate the existing and newly-developed models against data obtained at KTH and at other laboratories.

In 2004, several experimental programs, such as the COMECO (COrium MELt COolability), POMECO (POrous MEDIA COolability) and MISTEE (Micro-Interactions in STEam Explosion Experiments) programs were continued. The SIMECO (SIMulation of MELt Coolability) program was restarted in 2004. The construction of the POMECO-GRAND (POrous MEDIA COolability) facility was delayed due to lack of finances. However, existing POMECO facility was modified to study 3-D effects on debris coolability. In this report, the results from the COMECO experiment with high temperature oxidic melt, from the POMECO experiments for the multi-dimensional effects on debris bed coolability, from the SIMECO experiment for three-layer pool configuration and from the MISTEE experiments for steam explosion characteristics and loads are described. For analytical efforts, results from the COMETA code for the entire process of the steam explosions are discussed.

1 INTRODUCTION AND RESEARCH OBJECTIVES

Reactor safety's concern with severe accidents, since the TMI-2 accident led to almost twenty years of intense research efforts, which have resolved a number of severe accident issues which are related to containment performance. These include for example, LWR containment failure due to in-vessel steam explosions and direct-containment heating, BWR Mark I containment failure due to melt attack. Lately, research has been concentrated on accident management and a number of LWR plants, around the World, have adopted severe accident guidelines (SAMGs) and strategies. These include for instance, hydrogen control with igniters and catalytic recombiners, water addition to the Mark I drywell to prevent liner failure, vessel depressurization for DCH protection etc. There are still several severe accidents issues, which remain unresolved. A suggested prioritization [1] for the unresolved key issues is as follows:

- (1) In-Vessel and Ex-vessel Melt/Debris Coolability,
- (2) Ex-vessel Steam Explosion Loads,
- (3) Basemat Melt-Through,
- (4) Lower Head Failure Mode and its Timing, and
- (5) Core Quenching

Perhaps, the issue which most affects the mitigation strategy in the current plants is that of ex-vessel melt/debris coolability, since the stabilization and termination of the accident depends on it. The current SAM measures either avoid flooding the PWR vessel cavity and the BWR drywell or depend on such action for coolability, except that the flooding action opens the issue of the vulnerability of containment to steam explosion loads. Currently, neither mitigative measure is clearly preferred.

Therefore, the general objectives of the research we have performed at Royal Institute of Technology (KTH), Sweden in the research project MSWI (Melt-Structure-Water Interactions during Severe Accidents in LWRs) project under the auspices of the APRI program, jointly funded by HSK, SKI and the Swedish power companies are to obtain data and develop validated models for the resolution of five issues listed above. In the year 2004, the emphasis of the research work at KTH was placed on the experimental effort on phenomena and parameters, which govern the droplet fragmentations during the explosion phases of steam explosion, in-vessel and ex-vessel melt/debris coolability and melt pool convection. These experimental efforts were supplemented with analysis development efforts with the various codes including COMETA for steam explosion.

The specific objectives of each tasks have performed in the year 2004 are listed below.

In-Vessel and Ex-Vessel Debris Coolability (POMECO Program)

The POMECO facility at KTH is designed to investigate the coolability of a particulate porous debris bed simulated by sand beds. This year the POMECO experiments aimed to investigate the effect of multi-dimensional configuration of particulate debris beds, which have radial stratification on coolability since radially-stratified debris beds have been ob-

tained in the FARO tests after interaction of a melt jet with water. In doing so, the previous POMECO facility which modeled uniform and axially-stratified debris beds was modified. The modified POMECO facility has the same test section of the POMECO facility with additional heaters and radially stratified debris beds. In addition, Water entry into the bed is made from the sides of the bed in order to have a 3-D distribution of cooling. The facility employs more thermocouples to measure the local temperature transients in multi-dimensional debris bed configurations.

Specific phenomena associated with the configuration of radially stratified porous debris beds with multiple water injection are investigated; (a) quenching and dryout phenomena during top flooding, (b) effect of water injection at multiple locations at sides of the facility, (c) both top and bottom flooding using downcomers, (d) effect of non-condensable gas injection. The measured data are compared to those obtained in the previous debris bed experiments with homogeneous and axially stratified porous debris beds.

In-Vessel and Ex-Vessel Melt Coolability (COMECO Program)

The more realistic demonstration of coolability process has been tested in the COMECO facility at KTH, which employs high-temperature binary oxidic melt as corium simulant with internal heating. The main objective of the COMECO experiments in the year 2004 is to investigate the water ingress and coolability behavior of the melt pool with different kinds of flooding; such as top and bottom flooding. The COMECO facility employs one downcomer unit cell. The COMECO facility also employs the $\text{TiO}_2\text{-MnO}_2$ melt, which has a different material structure than that of the $\text{CaO-B}_2\text{O}_3$ melt. We believe that there may be differences in the water ingress efficiency in the melt pool due to material structure differences. The $\text{TiO}_2\text{-MnO}_2$ and CaO-WO_3 melts have ceramic structure when they cool down, while the $\text{CaO-B}_2\text{O}_3$ melt is of glass structure as it cools. There are also differences in the viscosity of these melts; the $\text{CaO-B}_2\text{O}_3$ melt has much higher viscosity. The COMECO experiments with different flow rates and subcooling will be tested. This program will continue into 2005.

Melt Pool Convection (SIMECO Program)

The SIMECO experiments in KTH had investigated the natural convection heat transfer at the boundaries of an internally heated stratified (two-layer) pool in the bottom head of the reactor vessel. In the year 2004, the SIMECO experiment investigated the natural convection heat transfer behavior in a three-layer stratified pool which was recently observed in the MASCA project.

Steam Explosion Loads (MISTEE Program)

The MISTEE experiments at KTH have been performed to investigate the characteristics of single drop steam explosion using advanced visualization techniques and measurement instruments. In the year 2004, the MISTEE experiments aimed to investigate the steam explosions with a single metallic melt droplet to evaluate the steam explosion energetics. At the same time, the uncertainty analysis to quantify the X-ray radiographic measurement is performed. The effect of thermo-physical properties of melts using various oxidic melts

are starting to be investigated. Preparation of melting and delivery methodology is also developed.

Steam Explosion Loads (COMETA Analysis)

A mechanistic computer code for steam explosion process, called COMETA, developed at JRC, Ispra, Italy, has been transferred to KTH, Sweden to systemically investigate the steam explosion processes in various geometries at different scales and to improve key models for steam explosions using database from the MISTEE experiments. In the year 2004, the COMETA analyses aimed to investigate the characteristic difference between two sets of steam explosion experiments with corium, i.e., those performed in JRC, Ispra, called FARO and the other in KAERI, Korea, called TROI. In contrast to the FARO tests, the TROI tests showed energetic explosions with corium composition.

2 PROGRESS OF RESEARCH PROGRAM

2.1 In-Vessel and Ex-Vessel Debris Coolability

2.1.1 POMECO Program

In this project, we investigated the influence of radial stratifications of the bed on the quenching using smaller size particles with prototypic porosity distribution, which has never been studied adequately in previous studies. These studies are important in order to bring further insight in debris bed quenching in stratified configurations and generation of data for model development and code validation. The most important task is to find out an effective method of quenching the heat generating debris bed. For this, we carried out experiments in a facility named as POMECO (PORous MEDIA COolability) as shown in Fig 2.1.1. The bed was composed of sand with lower porosity layer of particles at the center of test section and with higher porosity layer of particles at the periphery. The porosities and sizes of the sand particles chosen were close to those observed in a corium debris bed. The sand bed was heated volumetrically with power density closer to the decay heat generated in corium. To study the influence of non-condensable gases generated during an MCCI on quenching, two different gases such as air and argon were injected at the bottom of the bed during the quenching conditions. The gas flow rate was simulated to that actually generated during the later stages of MCCI from both basaltic and lime stone sand concretes.

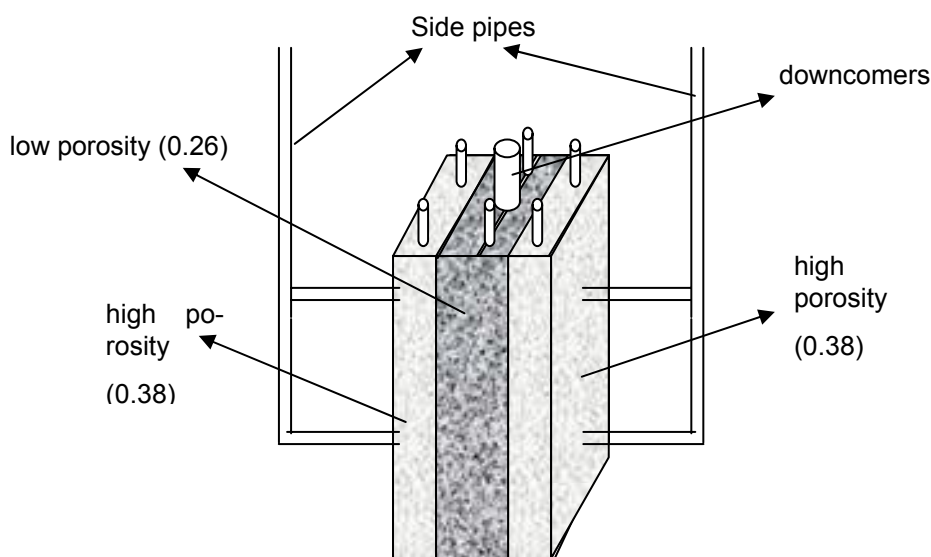
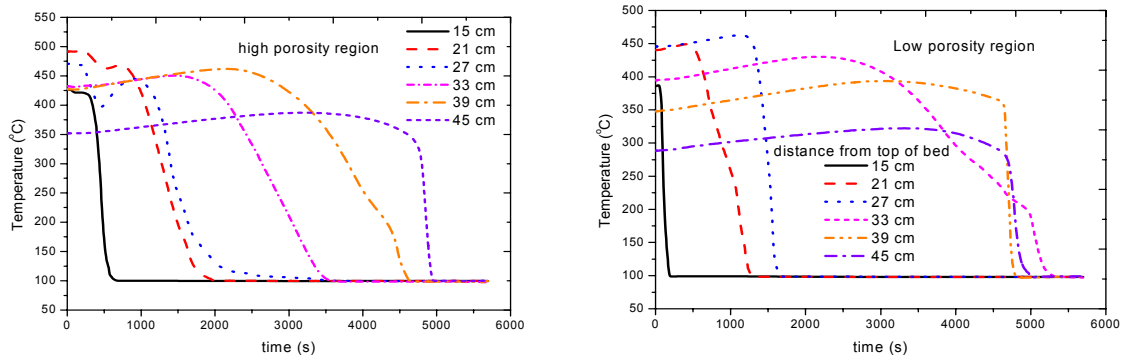


Fig.2.1.1 Schematic of POMECO facility

Experiments were conducted with and without gas injection rates when the bed was flooded from the top. It was found that top flooding alone might not be able to quench the bed even after many hours. To find out an effective method of quenching, water was injected at multiple locations from the side of the bed using side pipes. Besides, a series of experiments were conducted on the quenching of the bed with top flooding and bottom flooding using downcomers with and without non-condensable gases addition to the bottom of the bed. The size and location of the downcomers on the quenching behavior and their effectiveness on the quenching were investigated. Finally, the quenching period for

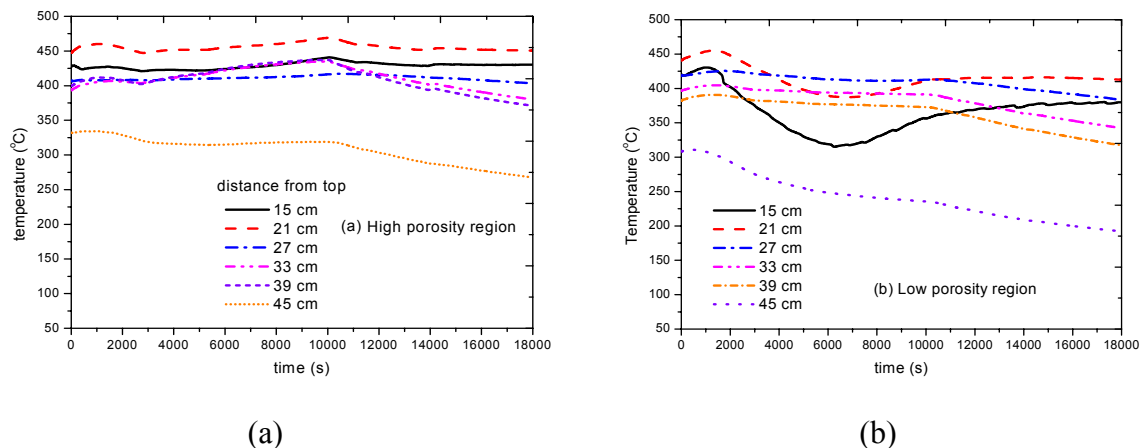
different conditions was measured and compared with that of a homogenous bed and axially stratified bed.



(a) (b)
Fig.2.1.2 Quenching behavior for top flooding

2.1.1.1 Top Flooding

For the top flooding tests, all downcomers were closed in the facility. After the bed was heated to an approximate average temperature of around 400 to 450 °C, water at a temperature of around 90 °C was flooded to the top of bed. The height of water column above the bed was nearly 0.5 m, which was kept constant throughout the test. Figs. 2.1.2 (a) and (b) show the typical temperature history in the bed in the high and low porosities regions respectively. The time period for quenching was found to be higher in the low porosity region (about 5300 s) as compared to that in the high porosity region (about 4950 s). Previous POMECO experiments showed that for a homogenous bed with the porosity of 0.26 and mean particle size of 0.8 mm, the quenching period was about 1650 s for top flooding.



(a) (b)
Fig.2.1.3 Effect of non-condensable gas on quenching (top flooding, air flowrate is 50 LPM).

When the porosity was larger (0.4) and the particle size was smaller (0.2 mm), the quenching period was about 9300 s, which is much longer than that with low porosity region. This implies that the quenching period is controlled more by the sizes of particle rather than the sizes of porosity. In the present case, the size of the low porosity sand and the high porosity sand was similar. So the difference in quenching period was mainly due to difference in the po-

rosities of the two layers. Moreover, it can be observed from the figures that the quenching behavior of the two layers are similar, i.e. the quenching first occurs at the top and then the front propagates to the bottom of the bed like that of a homogenous bed with top flooding. Hence there is no cross flow across the boundary between the two layers.

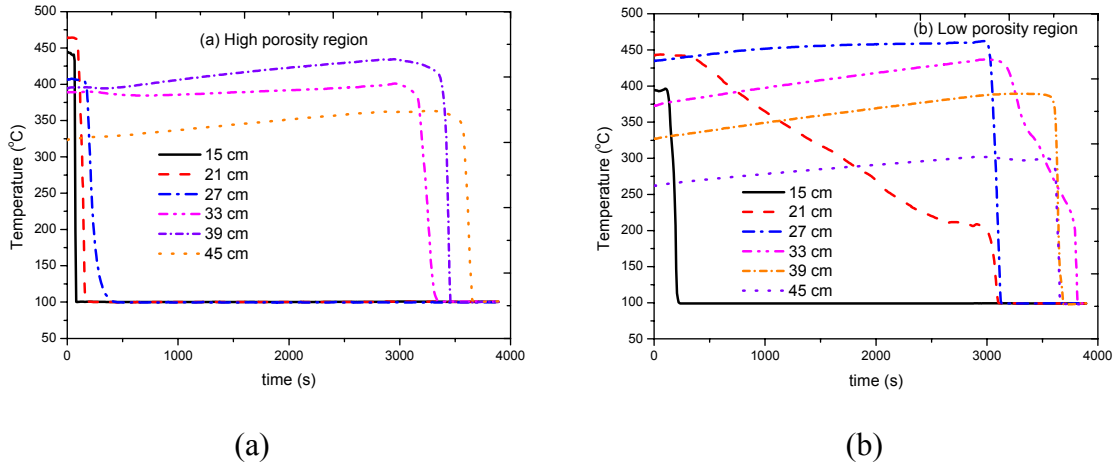


Fig.2.1.4 Quenching with top flooding and water injection at the side of bed

2.1.1.2 Effect of non-condensable gas injection on quenching

The effect of non-condensable gases on the quenching behavior with top flooding was studied which is shown in Fig. 2.1.3 for the high porosity and low porosity regions. The airflow rate was about 50 LPM. The quenching rate is negligible as can be seen from the transient temperature history of the bed. So CCFL conditions exist both in the low and high porosity regions. The slight cooling observed at the bottom of the bed, mainly in the low porosity region, is caused by convection heat removal due to the low temperature air.

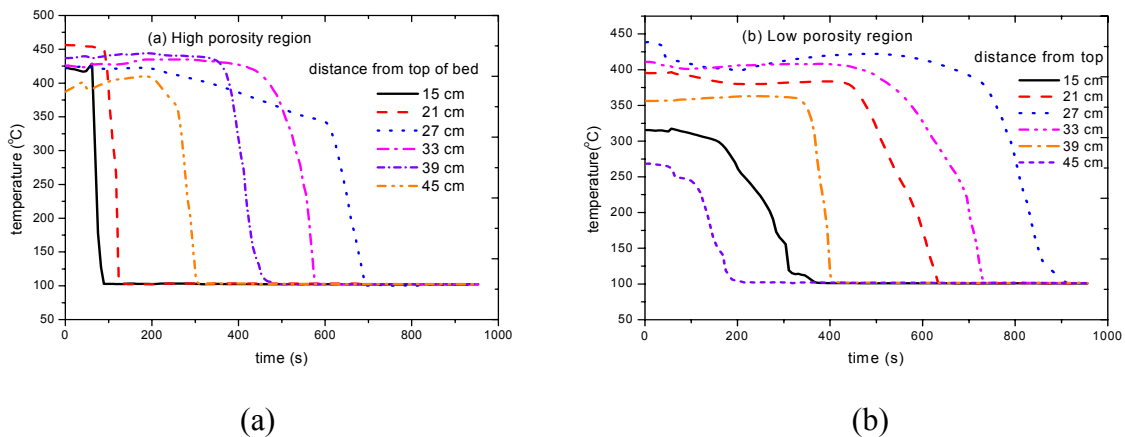


Fig.2.1.5 Quenching with top and bottom flooding using center downcomer.

2.1.1.3 Top flooding with side water injection

First, we investigated the quenching behavior of the bed when it was flooding from the top and at the same time water was injected using the side pipes. As shown in Fig.2.1.1, these side pipes inject water symmetrically in opposite side of the bed at four different points (two each side of the bed). The diameter of the side pipes is about 10 mm and the injection

points are at mm from the top of the bed. Fig. 2.1.4 shows the quenching behavior in the high and low porous regions respectively. The time period of quenching in the low porous layer was little higher than that in the high porous region similar to that observed during top flooding. However, the time period of quenching was reduced significantly with side pipe injection. Similar to that of top flooding, the quench front propagates from top to bottom of the bed in both low and high porous regions. But in the high porous region, the water penetration was found to be faster in the top layer of the bed (up to depth of 270 mm) as compared to that in the bottom layer of the bed.

2.1.1.4 Top and bottom flooding with the downcomers

Next, we investigated the quenching behavior of the bed with top flooding and bottom flooding using downcomers. First, the bottom flooding was carried out using the center large downcomer only and the other six small downcomers were closed. Figs. 2.1.5 (a) and (b) show the typical temperature behavior of the bed during quenching for the high porosity and low porosity regions respectively. The presence of downcomer in the center of the bed wherein the low porosity region is located helps in better quenching. But the time for quenching in the low porosity region is still found to be longer than that in the high porosity region. Comparing these results with that of with top flooding only, it is evident that bottom flooding helps in significant reduction of quenching period of the debris bed. Previous POMECO experiments reported a quenching time of nearly 1200 s for the homogeneous bed with porosity of 0.26 for the same mixture composition as used here. However, they employed a smaller downcomer with diameter 30 mm instead of 54 mm as used in the present case. Moreover, use of a large size downcomer along with presence of a larger porosity region in the periphery of the bed has augmented the quenching rate. The quench front propagates downwards from the top due to top flooding and upwards from the bottom of the bed due to bottom flooding simultaneously. The center region quenched at the end.

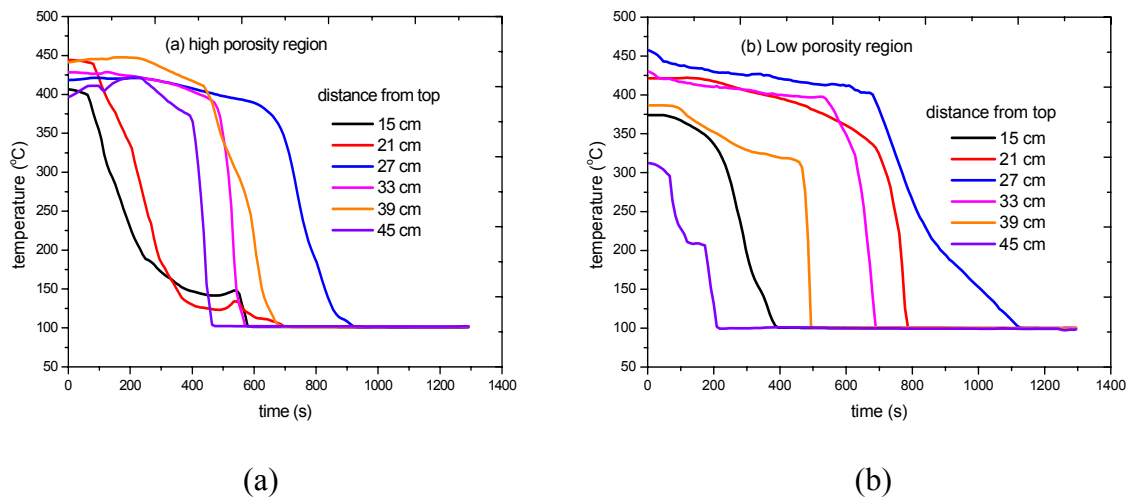


Fig.2.1.6 Quenching with top flooding and bottom flooding with small downcomers

Next, we investigated the effects of size of downcomers and their locations on the quenching rate. So instead of using a large downcomer, we put six small downcomers of size 12 mm symmetrically in the bed as shown in Fig. 2.1.1. These downcomers now are located at the periphery of the bed with two in the central low porosity region and two in each of the

peripheral high porosity regions. The center downcomer was closed. Figs. 2.1.6 (a) and (b) show the temperature variation in the bed during quenching for the high porosity and low porosity regions for the same radial and axial locations as described before.

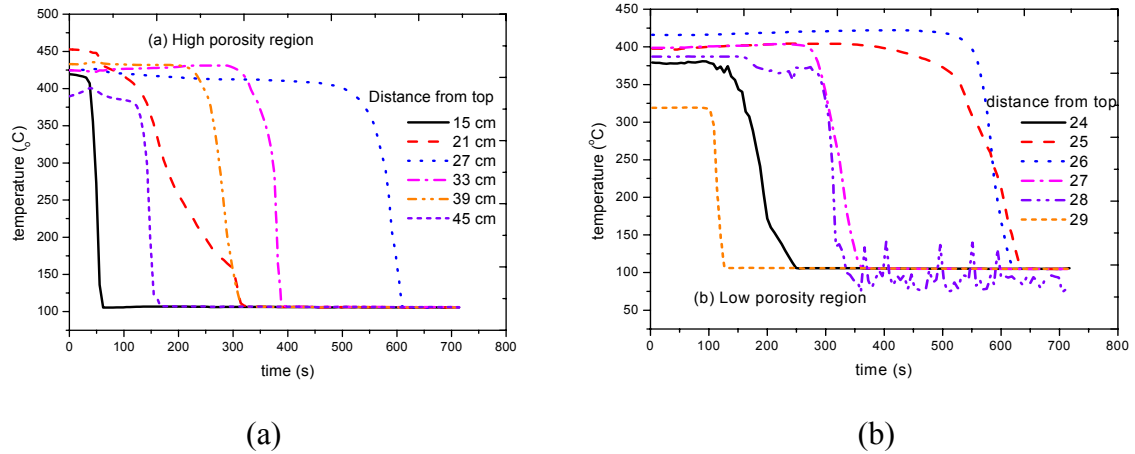


Fig.2.1.7 Quenching behavior with top flooding and bottom flooding with all downcomers

The time period of quenching for both low and high porosity layers are higher as compared to the previous case. The combined flow area of the six smaller downcomers is smaller as compared to the center large one. This may affect the bottom flooding rate and hence the quenching period. On the other hand, employment of all downcomers together (i.e. the six small downcomers and the center large one) reduces the quenching time significantly as shown in Figs. 2.1.7 (a) and (b). Another interesting feature of this result is that the difference in quenching rate in the low and high porosity regions is much smaller unlike the previous cases.

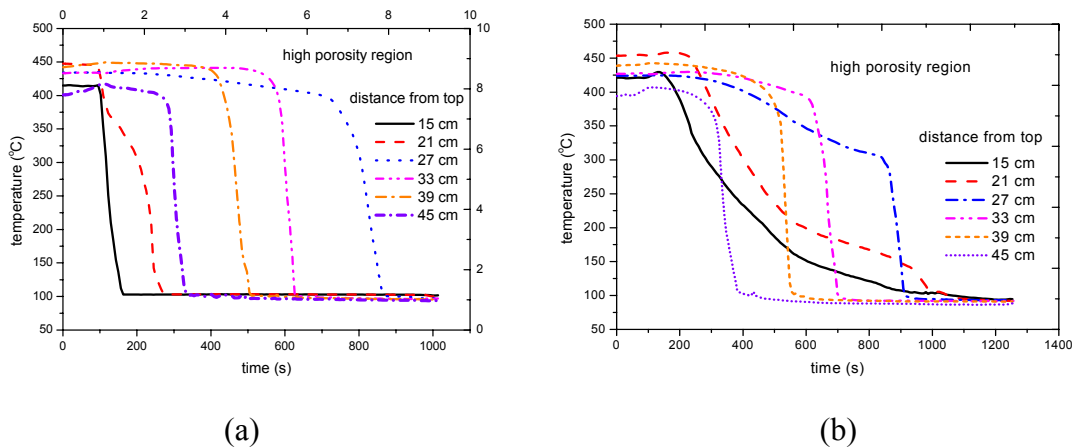


Fig. 2.1.8 Effect of non-condensable gas on quenching (top flooding and bottom flooding with all downcomers, air flow rates are (a) 50 and (b) 125 LPM).

Hence from the above results it is evident that the quenching of a heat generating radially stratified bed may not be effective with top flooding alone when especially the debris bed is generating non-condensable gases due to MCCI. Of course, with water injection at the periphery of the bed reduces the quenching period, however, the most effective means of quenching of the bed can be achieved by bottom flooding of the bed using downcomers in

addition to the top flooding. These downcomers provide an effective passive means of removing the decay heat by two-phase natural circulation.

The effects of non-condensable gas on quenching during top and bottom flooding conditions were studied for different airflow rates. Fig. 2.1.8 shows the quenching rate for two different airflow rates in a high porosity layer, when all downcomers were open. There is a systematic increase in quenching time with increase in airflow rate observed at all axial locations. The overall quenching time is also higher as compared to the case when no air was injected (Fig. 2.1.7(a)). Similar behavior is also observed in a low porosity region. The non-condensable gases trigger the CCFL and hence affect the flooding.

The effect of non-condensable gases on quenching behavior when the center downcomer is only opened can be seen in Figs. 2.1.9 (a) and (b) for the high and low porosity regions respectively. The quenching rate is delayed both in the low and high porosity regions with non-condensable gas injection. But one interesting observation here is that in the high porosity region, the quenching front propagates from top to bottom like the case with top flooding. It means, the air does not allow water to penetrate to the bottom of the bed earlier unlike the previous case or that without air injection (Fig. 2.1.3 (a)). But in the low porosity region, the penetration of air into the bed is more difficult and hence it does not affect the quenching characteristics significantly.

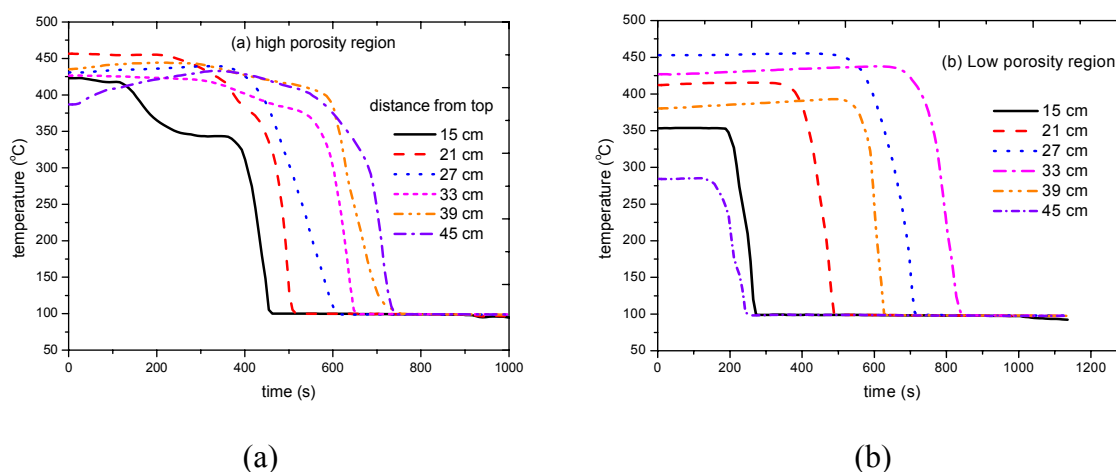
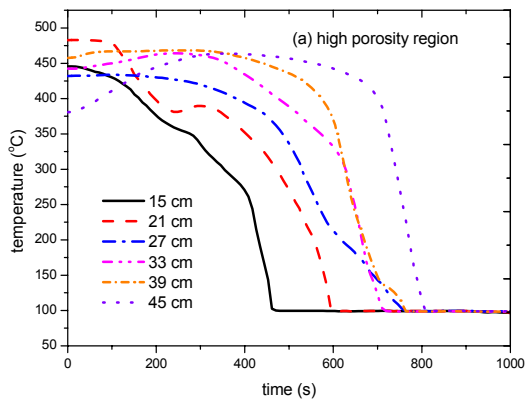
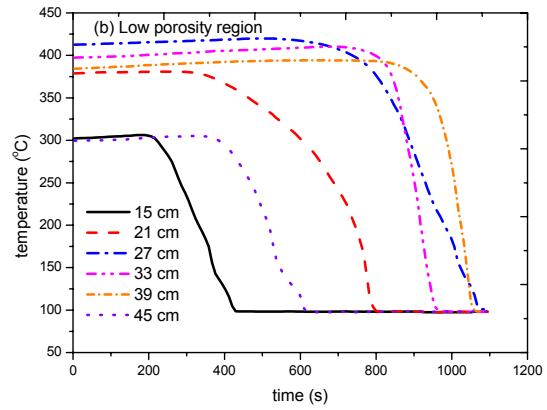


Fig. 2.1.9 Effect of the non-condensable gas on quenching (top flooding and bottom flooding with center downcomer only), air flow rate is 50 LPM

In order to understand the effects of gas properties on the quenching behavior, we injected argon which is about 20 % heavier than air and repeated the quenching experiments with top flooding and bottom flooding with center downcomer open only, which were already performed with air. Fig. 2.1.10 shows the quenching behavior of the bed with Argon flow rate of 40 LPM in both low and high porosity regions respectively. This flow rate corresponds to approximately the mass flow rate for 50 LPM of air. The time period of quenching in the high porosity region was same as that in the air where as in the low porosity region, the quenching rate with argon was found to be little smaller. Unlike in the low porosity region, the quench front propagation in the high porosity region was found to take place from top to bottom similar to that with air. The quenching rate in the top layer was also found to be smaller as compared to that in the bottom layers in the high porosity region.



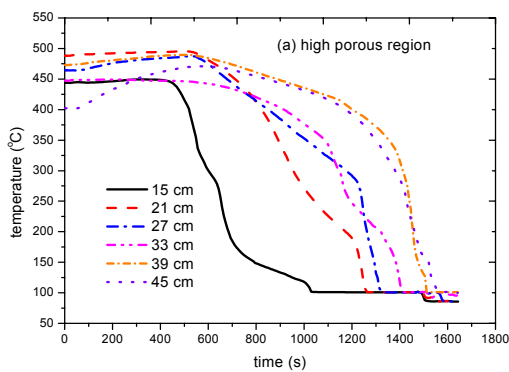
(a)



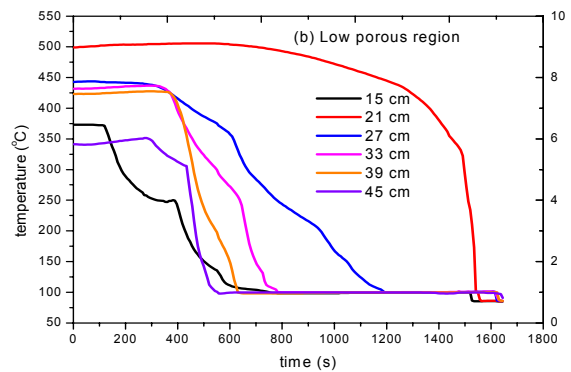
(b)

Fig.2.1.10 Quenching behavior with argon injection (top flooding and bottom flooding with downcomer, argon flow rate of 40 LPM)

Fig. 2.1.11 shows the quenching behavior of the bed when argon at a flow rate of 100 LPM was injected at the bottom of the bed. This corresponds to nearly 120 LPM of air. The time period of quenching was found to be longer than that observed with air both in the high and low porous regions. The quench front propagation was found to be similar like that of the previous case, i.e. flow rate of 40 LPM. Moreover, it is found that higher the flow rate of the non-condensable gas, longer is the quenching period. Another interesting observation is that the quenching period for the top region is found to be longer in the high porous region as compared to that in the low porous region because of the non-condensable gases which prefer to flow in the low resistant high porous region. Hence, there is more chance of CCFL in the high porous region for larger flow of non-condensable gases even though bottom flooding is done using a large size downcomer at the center of the bed.



(a)



(b)

Fig.2.1.11 Quenching behavior with argon injection (Top flooding and bottom flooding with center downcomer open only, argon flow rate of 100 LPM)

2.1.2 COMECO Program

In the year 2004, one experiment was carried out with the melt prepared from the binary oxide mixture of CaO (30% by wt.) and B₂O₃ (70% by wt.), which has properties similar to the prototypical material during the later phase of the severe accident. The schematic of the experimental facility is shown in Fig. 2.1.12. The test facility consists of a test section of 200x200x300 mm³ and the test section was heated from outside using special type of Mo-Si heaters to simulate the decay heat. About 14 litres of melt was poured into the test section before it was flooded with water from the top. The steam flow rate was measured using venturi meters, which give an estimation of the quenching rate. A total of 24 K-type thermocouples were employed to measure the temperature at three different radial locations.

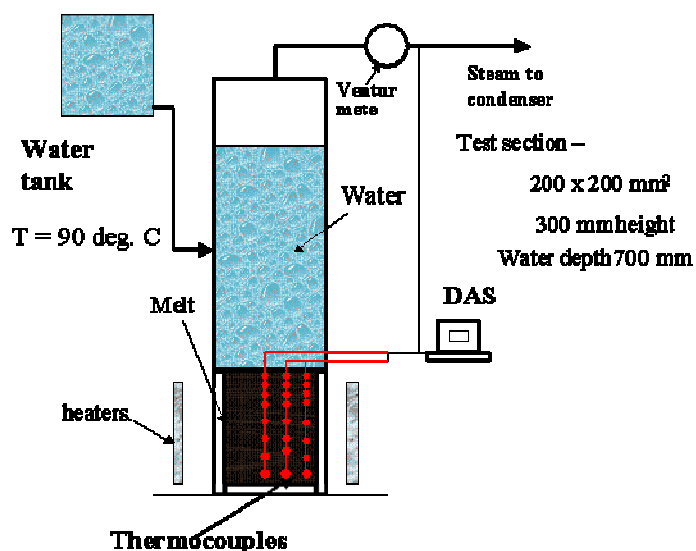


Fig.2.1.12 Test Facility for COMECO Experiments

Fig. 2.1.13 shows the temperature of the melt at various locations during the experiment. Fig. 2.1.14 shows the temperatures during the initial period of the experiment. As we can see the temperature of the melt in the first three locations from the top drops down to the saturation temperature of water due to water ingress. The temperature at the fourth location from the top (which is about 122 mm) is also found to drop from the initial temperature due to heat conduction from the melt to the overlaying water. The water ingress was not observed at this location.

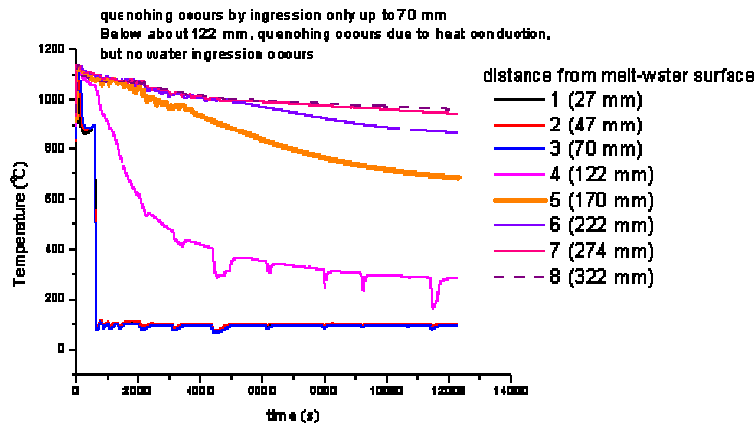


Fig.2.1.13 Quenching of melt during experiments

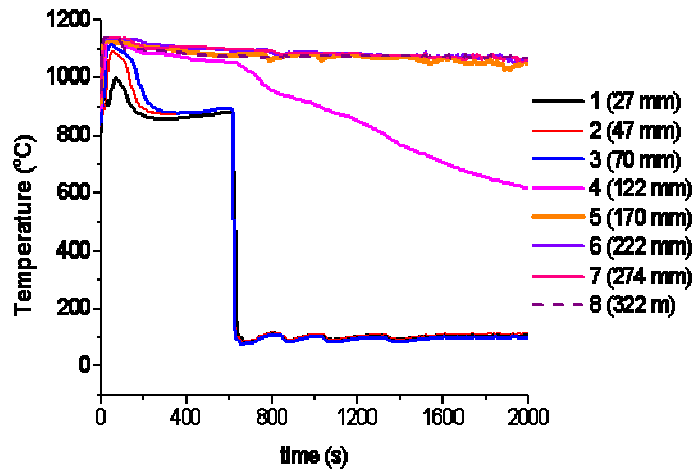


Fig.2.1.14 Quenching behavior in the initial period

Figs. 2.1.15 and 2.1.156 show the temperatures of the melt at the other radial positions. They also exhibit similar quenching behavior as in the first radial position. Fig. 2.1.17 shows the steam flow rate measured during the experiment. The flow rate is high during the initial quenching process and later on decreased to a very low value. Figs. 2.1.18 (a) and (b) show the melt structure after the test was over. The crust formed was cut axially from top to bottom. Fig. 2.1.18(a) shows that the crust has a solid rock like structure with no porosity inside. Whereas a lot of fragmented pieces are observed in the top portion (Fig. 2.1.18(b)), which confirms the water ingress up to the depth mentioned previously.

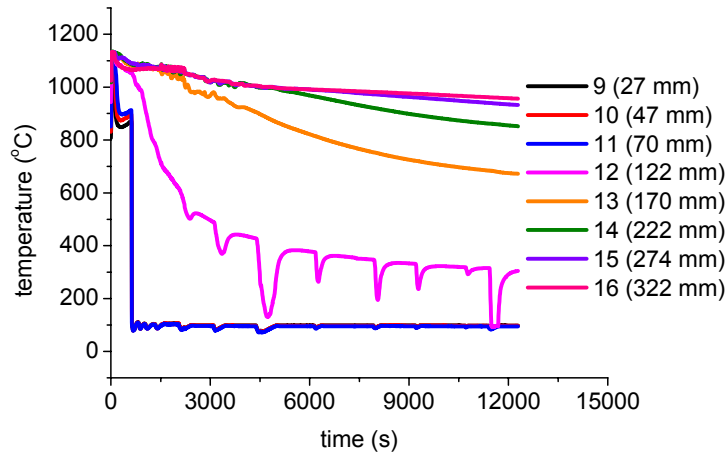


Fig.2.1.15 Quenching of melt at second radial position during the experiment

In the year 2004, experiments with 8%MnO+22%TiO₂ melt were also conducted. Recently attempts with MnO+TiO₂ melt were failed due to the high temperature of the melting point of the mixture and it is difficult to achieve with the existing furnace. The unexpected failure of the melt generator and heating system in the COMECO facility was occurred during the first experiment for the melt coolability with the very high-temperature binary oxidic melt, MnO+TiO₂ whose liquidus temperature is 1380 °C. The temperature of the crucible inside the induction furnace reached ~ 1500 °C which caused it structural failure. The capacitor and electric unit within the induction furnace overheated and failed. Two heaters in the COMECO facility also failed during experiment and dismantling. In this period of the project, the COMECO melt generation system was under repair. It is expected that some delay on the COMECO experiments for ex-vessel coolability of molten pool will occur due to the failure of the induction melt generator system.

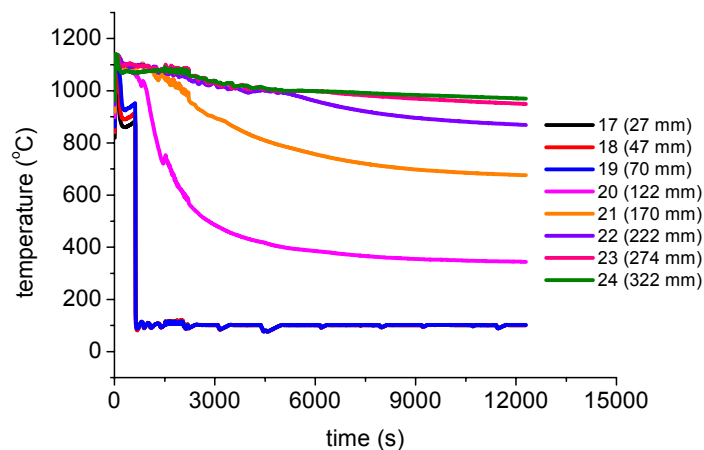


Fig.2.1.16 Quenching of melt at third radial position during the experiment

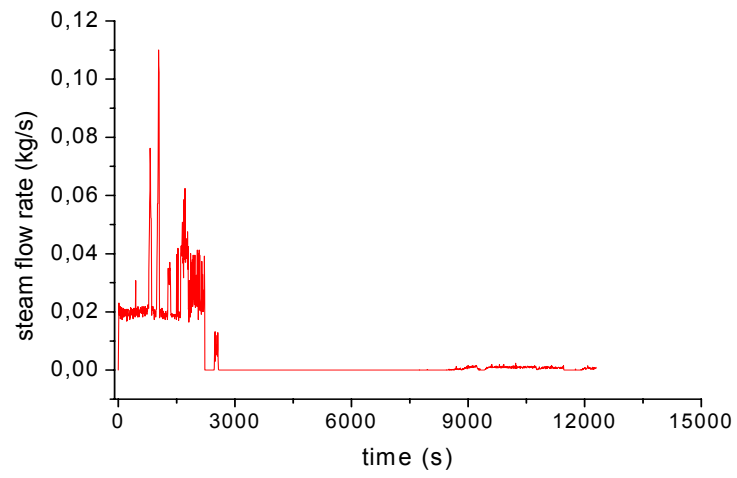


Fig.2.1.17 Steam flowrates during the experiment



Fig.2.1.18 Photos for (a) axial view and (b) top portion of melt structure after the experiment

2.1.3 SIMECO Program

A hypothetical core melt accident in a light water reactor may result in accumulation of core debris in the lower head of the reactor pressure vessel. If the core debris is unquenched, it will heat up due to the internal heat generation and forms a melt pool. The core melt pool formed consists of a oxidic region at the bottom and a metal layer on the top. The thermal loads exerted on the vessel wall by the natural circulation in the pool have been studied for many years. The primary interest was the assessment of the feasibility of an accident management scheme to retain the melt within the lower head by cooling the vessel outside wall with water. The RASPLAV Program conducted in Russia, employed prototypic ($\text{UO}_2\text{-ZrO}_2$) melt materials in a 200 kg slice facility to study the thermal loads imposed by the prototypic melt on a cooled vessel wall. These experiments confirmed that the natural convection heat transfer behavior in prototypic melt was similar to that observed in simulant materials. In order to investigate the effects of stable stratification on the heat transfer of the lower curved boundary of a reactor vessel and to the top boundary of the liquid pool, the SIMECO Program was extended in the year 2004. This program consists of performing experiments on convection in stratified pools with internal heat generation. Previously, one- and two-layers experiments were performed in the SIMECO facility.

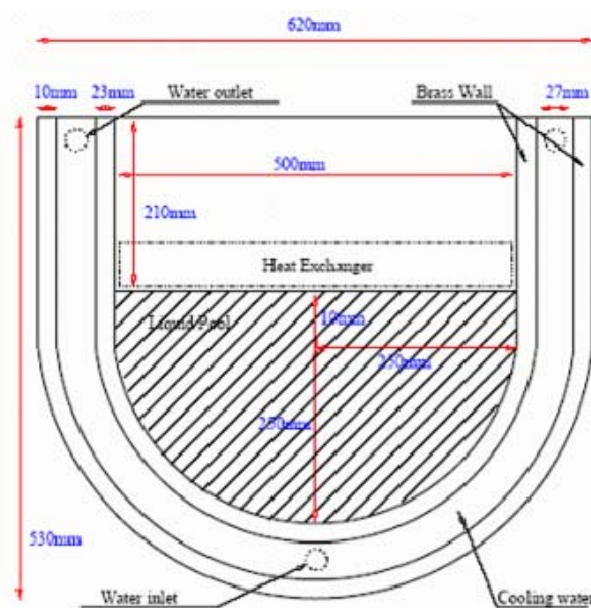


Fig.2.1.19 Schematic of SIMECO facility

2.1.4 SIMECO Experiment

The SIMECO experimental facility consists of a slice type vessel, which includes a semi-circular section and a vertical section, representing the lower head of the reactor vessel. The size of the facility is scaled to be 1/8 of prototype PWR type reactors. Fig. 2.1.19 shows a schematic of the facility. The diameter and height of the test section are respectively 62.0 cm and 53.0 cm. The width of a slice is 9.0 cm. The front and back faces of the facility are insulated in order to decrease heat losses. Thickness of the vessel wall is 2.3 cm. The vessel's sidewall represented by a thick brass plate, is cooled by a regulated water

loop. On the top of the vessel a heat exchanger with regulated water loops is employed to measure the upward heat transfer. The sideways and downward heat fluxes are measured by employing array of thermocouples at several different angular positions. Practically isothermal boundary conditions are provided at pool boundaries. Cable type heater with 3 mm in diameter and 4 m in length provides internal heating in the pool, inside the vessel. A heat exchanger mounted on the exit of cooling water, is employed to increase cooling capacity of the water. The isothermal bath is designed to provide constant temperature. A circulation pump was mounted in order to establish necessary flow rate. One digital and one analog flowmeters are mounted to control water flow through the wall of the slice, while one analog flowmeter is controlling the flow in the upper heat exchanger. Total number of 64 K-type thermocouples is mounted to obtain the data on average heat flux on the sidewall and on the top of the pool, inlet and outlet water temperatures, as well as temperatures inside the vessel, and the upper heat exchanger.

2.1.4.1 Two-layer simulations

Paraffin oil and water were used as simulants for the stratified two immiscible fluids in the pool. Paraffin oil with lower density was put on the top of the water layer. Choice of these simulants is determined by different factors such as specific heat coefficient, miscibility, toxicity, as well as density. The density difference between paraffin oil (880 kg/m³) and water (999.1 kg/m³) is about 12%. These ratios were closer to that of prototypic melt layers observed in the RASPLAV program.

The height of the lower pool (water) was kept constant at 22 cm, and the thickness of the upper layer (paraffin oil) was kept 5 cm. The heater is located on the 4 cm elevation, and has height of 20 cm, so the heat was supplied partly to the water layer (18 cm), as well as partly to the upper layer – paraffin oil (2 cm). Cooling water mass flow through the side-wall was chosen to be 8.5 l/min, and the mass flow in the upper heat exchanger is kept at 3.0 l/min. The heater power was varied from 900 W to 1300 W. The corresponding Rayleigh number (Ra) was estimated by the relation as given by

$$Ra = \frac{g\beta Q_v H^5}{\alpha \nu k} \quad (2.1.1)$$

which is found to be in range from 6.01×10^{12} to 8.7×10^{12} in these experiments so that turbulent convection is clearly established in the liquid pool. Values of all the properties are taken for the pool average temperature at steady state.

2.1.4.2 Three-layer simulations

Paraffin oil, water, and chlorobenzene, were employed as simulants for stratification of three immiscible fluids. As said before, choice of these simulants is determined by different factors such as specific heat coefficient, miscibility, toxicity, as well as density. The density difference between paraffin oil (880 kg/m³) and water (999,1 kg/m³) is about 12%, and between water and chlorobenzene (1106 kg/m³) is about 11%.

The height of the lower pool (chlorobenzene) was kept constant at 4 cm, the thickness of the middle layer (water) is 18 cm, and the thickness of the upper layer (paraffin oil) was 5 cm. Since, the heater is located on the 4 cm elevation, and has height of 20 cm, so the heat was supplied to the whole middle layer, as well as partly to the upper layer (2 cm), as in case of two-layer tests. The bottom layer is kept unheated. Cooling water mass flow

through the sidewall was kept equal to 8.5 l/min and the mass flow in the upper heat exchanger was kept at 3.0 l/min. The Rayleigh number (Ra) ranges from 6.01×10^{12} to 8.7×10^{12} , the same as in case of two-layer experiments. Therefore, there is turbulent convection in this set of experiments as well. Each experiment was started with three separated layers as the initial condition. Then the experiment is continued until the steady state was reached, which is defined as a global heat balance greater than 90%, and a thermal evolution lower than one degree per hour.

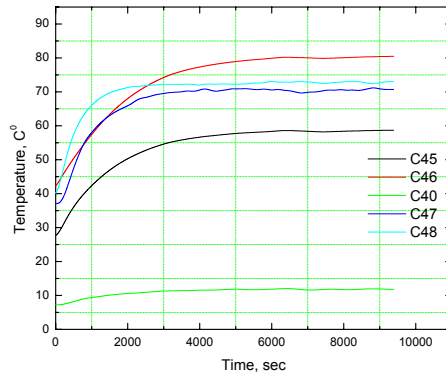


Fig. 2.1.20 Temperature profile inside two-layer pool at $Ra=6.01 \times 10^{12}$

2.1.4.3 Steady-state temperature distribution in the liquid pool

The temperature distribution in the liquid pool has been measured, by means of thermocouples, mounted along the centerline of the vessel. Typical temperature field profile along the center of the pool during the whole experiment is shown in the Fig. 2.1.20.

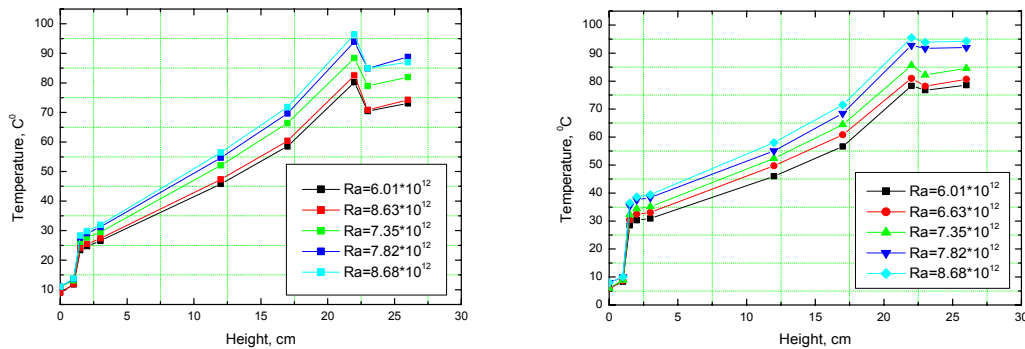


Fig.2.1.21 Temperature field inside the vessel (centerline) in (a) two-layer experiments and (b) three-layer experiments

Similar tests were conducted at different powers. The temperature field inside the pool during steady state is shown in Fig. 2.1.21(a) for these powers and the corresponding Rayleigh numbers are also shown in the figure. It can be observed that the temperature rises gradually along the height of the pool, until it reaches the interface between two upper liquids, i.e. water and paraffin oil. At that point the temperature suddenly drops due to the interface resistance to the upward heat flow. Then there is a slight increase in temperature in the upper paraffin layer due to convection.

Similar temperature distribution is observed in the three-layer experiments as shown in Fig. 2.1.21 (b). However, the temperature drop at the interface between the water and paraffin oil is found to be smaller in case of three layer experiments as compared to that in the two layer experiments at a given power. This shows that the thermal resistance is lower for a pool with chlorobenzene. A significant difference to be mentioned is the higher temperature rise in the bottom chlorobenzene layer (below 5 cm). The maximum pool temperature for both experiments is almost the same, but there is difference between temperature values in the bottom of the vessel which could be due to the difference in thermal physical properties between water and chlorobenzene.

2.1.4.4 Heat flux distribution in the sidewall

The heat flux was estimated from the measured temperature distribution along the sidewall as given below.

$$q = -k \frac{T_{wall} - T_p}{dx} \quad (2.1.2)$$

This is determined for different Rayleigh numbers for both two and three layer tests.

Fig. 2.1.22(a) shows the heat flux distribution along the vessel wall in the two layer experiments. It can be seen from Fig. 2.1.22(a) that the maximum heat flux is observed around in the region of 57 degrees, suffering from maximum thermal load. The heat flux increases along with the radius, reaching its maximum, and then decreases again in the upper part of the sidewall.

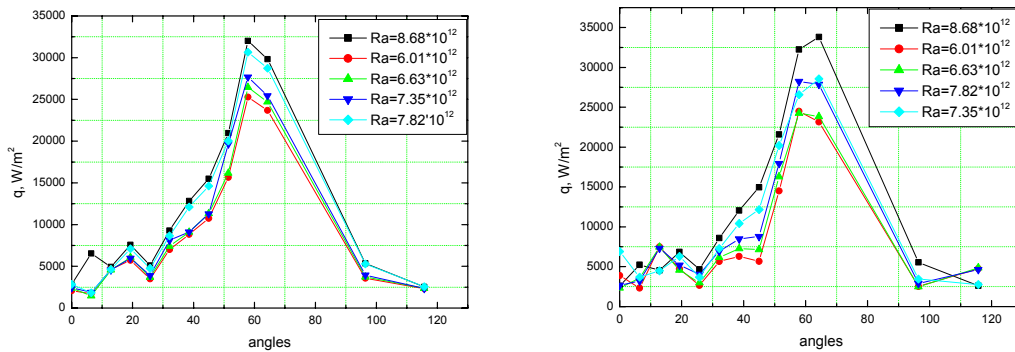


Fig.2.1.22 Heat flux distribution in the side wall for (a) two-layer experiments and (b) three-layer experiments

Similar results are seen for the heat flux distribution in case of three layer experiments as shown in Fig. 2.1.22(b). However, at higher Rayleigh numbers ($Ra=7.82 \times 10^{12}$, and $Ra=8.68 \times 10^{12}$), the maximum heat flux is observed around 64 degrees, which is different from what we had obtained, from two-layer experimental results. But for lower Ra numbers ($Ra=6.01 \times 10^{12}$ to 7.35×10^{12}), the location of peak heat flux remains almost the same. Apparently, one can observe that at low Raleigh numbers there is less heat directed to the side wall in the lower parts of the vessel in three layer experiments as compared to that in two layer experiments. This can be explained by the existence of the lower chlorobenzene layer in place of water in three-layer experiments, which helps in better heat diffusion and redistribution. However at high Raleigh numbers the heat flux distributions in the lower part of vessel are similar.

2.1.4.5 Upward and downward heat fluxes

Another important issue is to investigate and discuss the upward and downward heat fluxes in the vessel during transient convection. In order to understand the cooling mechanism, we are introducing the Q_{up}/Q_{down} characteristic ratio, which was calculated for both two- and three-layer experiments.

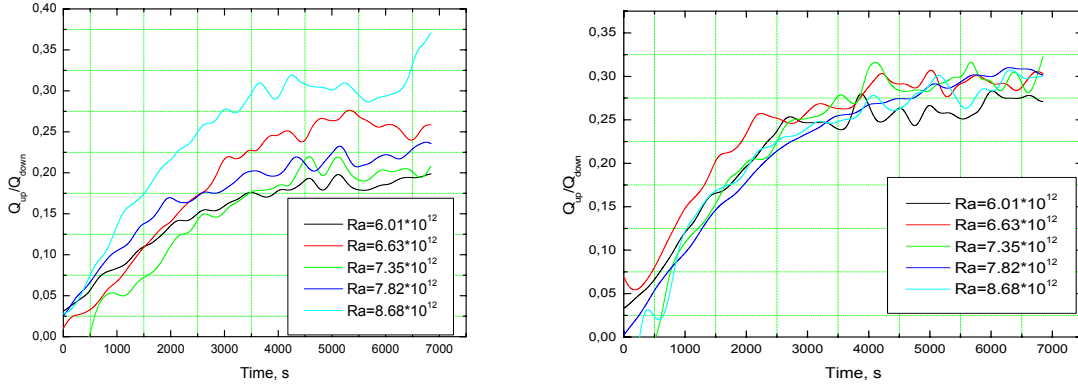


Fig.2.1.23 The Q_{up}/Q_{down} ratios in (a) two-layer experiments and (b) three-layer experiments

Fig. 2.1.23(a) shows the transient Q_{up}/Q_{down} ratio at different powers for two layer experiments. The highest upward to downward heat transfer rate is observed at $Ra=7.82 \times 10^{12}$, and the lowest at $Ra=6.01 \times 10^{12}$. Moreover, it is evident that the downward heat transfer rate is much larger than the upward heat transfer rate because of presence of interface resistance. For experiments with three stratified layers pool, we can observe in Fig.2.1.23(b) that the Q_{up}/Q_{down} ratio is almost similar for all cases. One still can see that the higher the Ra number the higher is the heat transfer rate, but the difference is marginal.

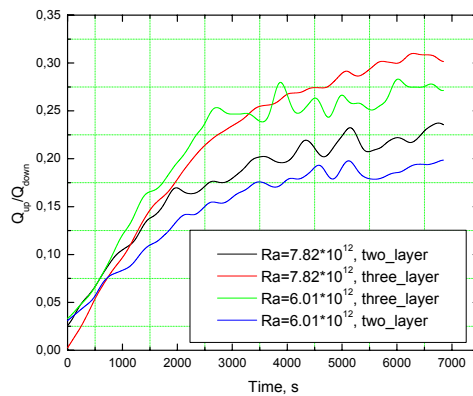


Fig.2.1.24 Comparison of Q_{up}/Q_{down} ratios in two-layer and three-layer experiments

Fig. 2.1.24 shows the comparison of the Q_{up}/Q_{down} ratio for both two and three-layer cases under the same Ra number. One can easily observe that the upward heat transfer for three layer experiments is higher, than that for two-layer experiment for the same power input.

This can be due to the lower thermal resistance in the three-layer pool, which allows the heat to be directed up. Previous experiments with two miscible fluids showed the $Q_{\text{up}}/Q_{\text{down}}$ ratio increased to the value of 1.5 when the layers mixed. However the experiments with immiscible two- and three layers show that when there are separate layers with interfaces, there is a large resistance to the heat flow upwards and the $Q_{\text{up}}/Q_{\text{down}}$ values are in the range of 0.2 to 0.4 only.

2.2 Ex-Vessel Steam Explosion

2.2.1 MISTEE Experimental Program

2.2.1.1 Metallic melt tests

In the year 2004, a series of metallic tests with Tin as a simulant melt has been conducted to refine the quantification of X-ray images and to build database for the comparison to tests with oxidic melts. To investigate the ability of nanofluid as a steam explosion suppression agent, a series of film boiling experiments with a high-temperature stainless sphere which quenches in nanofluid with various concentrations was conducted. Development of techniques to prepare and deliver a single droplet of various high-temperature oxidic melts for oxidic melt tests was a focus in the last period of the year 2004. In analytical efforts, the COMETA code has been successfully installed at KTH and performed a series of verification runs against the experimental data obtained from the FARO and the KROTOS tests in JRC-Ispira, Italy and from the TROI tests, in KAERI, Korea, were performed.

A facility, called **MISTEE** (**M**icro **I**nteractions in **S**tream **E**xplosion **E**xperiments) shown in Fig. 2.2.1 with a continuous high-speed X-ray radiography system is used for the single drop vapor explosion experiments. Molten tin mass of 0.7g is chosen in this series of tests to guarantee the delivery of a single drop into water through the crucible bottom hole. The external trigger, located at the bottom of the test chamber, is a piston that generates a sharp pressure pulse similar to a shock wave. The trigger hammer is driven by a rapid discharge of a capacitor bank, consisting of three capacitors that impact on the piston to generate a pressure pulse.

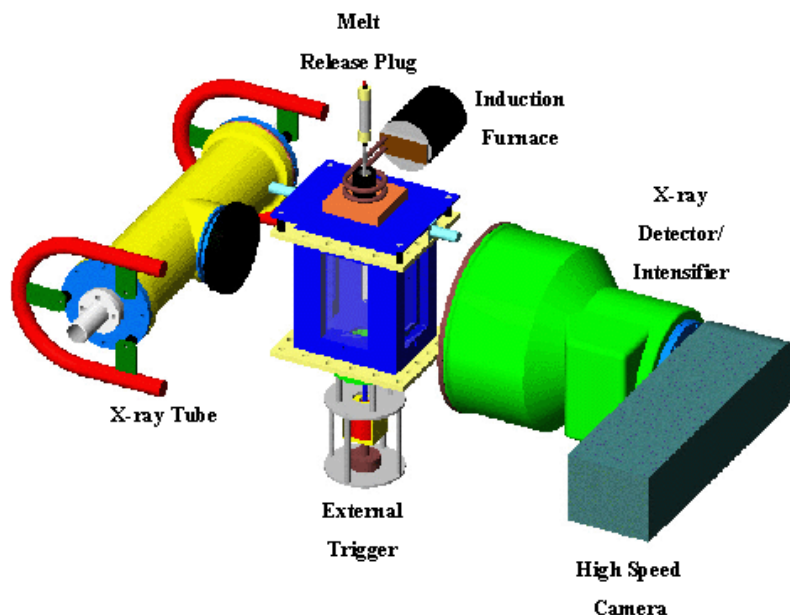


Fig.2.2.1 Schematic of MISTEE Facility.

The visualization system of photography and radiography consists of a continuous X-ray source tube (max. 320 keV, 22mA), an X-ray converter and image intensifier and a high-speed video camera (max. 8000fps for 4 s). The resolution of the X-ray image is 56 line pairs per centimeter. The image size of the high-speed camera at 8000 fps is 80x70 pixels.

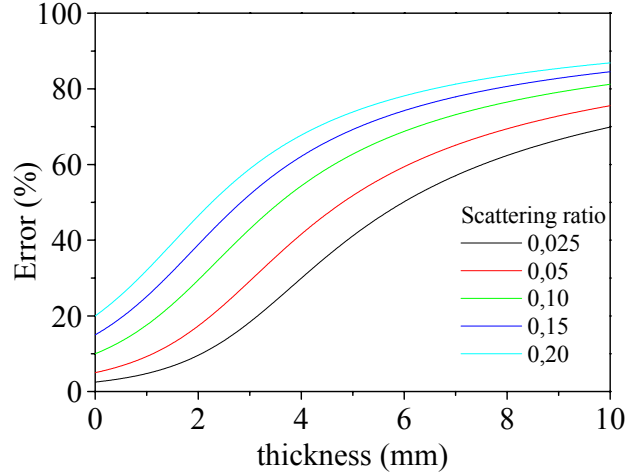


Fig.2.2.2 Error dependent on the tin thickness and scattering ratio.

The uncertainty involved in the quantification of X-ray visualization has been analyzed. In general, the intensity of the detected X-rays, I , after the transmission of the incident X-ray beam, I_0 , in a medium, obeys the attenuation law as follows

$$I = I_0 \exp\left\{-\sum_i \mu_i \delta_i\right\} \quad (2.2.1)$$

where, δ_i and μ_i are the thickness and the mass attenuation coefficient of i -th materials. The total X-ray intensity detected at the converter, however, consists of the intensity of the X-rays that penetrated through the test section and were attenuated, I^A , and the intensity of the X-rays that were scattered by the object and surrounding shields I^S ; $I = I^A + I^S$. The image contrast, proportional to the transmitted X-ray beam, is transformed into digitized gray levels. Therefore the digitized gray level, G , can be generally expressed as,

$$G = \alpha I + G_{DC} = \alpha(I^A + I^S) + G_{DC} = \alpha I_0 \exp\left\{-\sum_i \mu_i \delta_i\right\} + G^0 \quad (2.2.2)$$

where α , G_{DC} , and G^0 are the proportional constant, dark current of the imaging system and the image offset, which represents the gain of the image gray level due to the scattered X-rays and the CCD dark current, i.e., $\alpha I^S + G_{DC}$, respectively. The basic arrangement of our XR system (X-ray tube and converter) with a test section that has multiphase mixture of water, vapor and melt during the vapor explosion process. Combining the equations, the normalized gray level of the image can be expressed in terms of the thickness of the melt droplet as,

$$\Delta G \equiv \frac{G_M - G^0}{G_{NM} - G^0} \cong e^{\{-\mu_M \delta_M\}} = \beta e^{\{-\mu_M \delta_M\}}. \quad (2.2.3)$$

Fig. 2.2.2 shows the error in respect to the tin thickness and scattering ratio, for the current X-ray settings of our system (120 kV). For such high energy X-rays, scattering is of great importance and must be taken into account. The scattered photons create a loss of contrast and definition, resulting in large measurement errors. The average gray levels in a row,

transverse direction, shows a quite low fluctuation, around 4.8%, but on the average in a column, longitudinal direction, it rises to around 29%.

The non-uniformity of the background is due to the camera noise (dark current), uneven illumination through the image (output screen response and intensity distribution of X-ray radiation – maximum in the center) and CCD response to light (each pixel response varies). That means that the background subtraction and offset correction should be performed pixel by pixel and not using an average number.

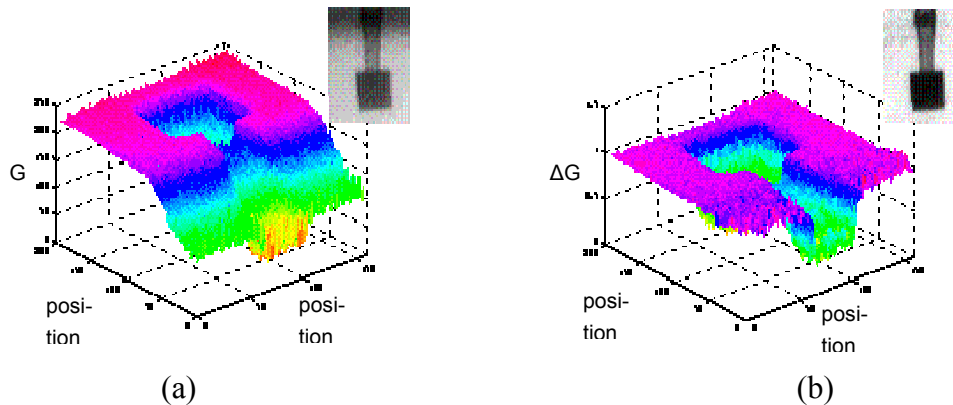


Fig. 2.2.3 (a) tin phantom gray level; (b) tin phantom after image processing

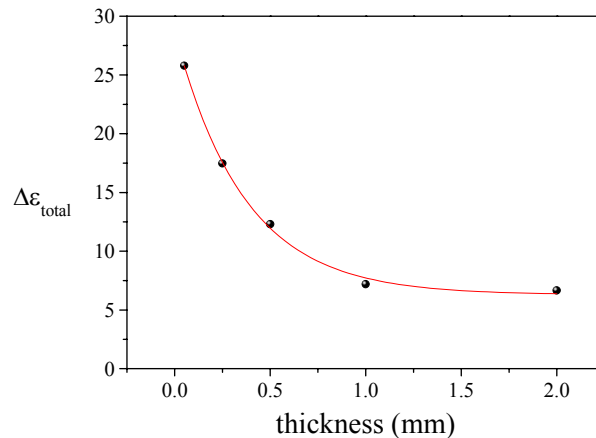


Fig. 2.2.4 Total uncertainty of the measurement.

Figure 2.2.3(a) shows the brightness distribution of the radiography image of a tin piece, and Figure 2.2.3(b) shows the same image after G^0 correction. It is clear the significant reduction of the image noise, has been achieved.

- Fluctuation of the optical brightness between pixels $\Delta\epsilon_{pixel}$
- Contrast ratio on the fluorescent screen $\Delta\epsilon_{screen}$
- Deviation between the actual and measured thickness, $\Delta\epsilon_{\delta}$
- Statistical error of the X-ray beam $\Delta\epsilon_{stat}$

The achievable measurement accuracy depends on the statistical error of the X-ray beam $\Delta\epsilon_{stat}$, contrast ratio on the fluorescent screen $\Delta\epsilon_{screen}$, on the fluctuation of the optical brightness between pixels $\Delta\epsilon_{pixel}$, and the deviation between the actual and measured thickness, $\Delta\epsilon_{\delta}$. The correlation for the total uncertainty $\Delta\epsilon_{tot}$ is given by:

$$(\Delta\epsilon_{tot})^2 = (\Delta\epsilon_{stat})^2 + (\Delta\epsilon_{screen})^2 + (\Delta\epsilon_{pixel})^2 + (\Delta\epsilon_{\delta})^2 \quad (2.2.4)$$

As shown in Fig. 2.2.4, for a higher thickness the error decreases, this can be explained by the fact that the optical brightness approaches its saturation, represented by the asymptotic part of the calibration curve, giving an almost constant gray level. For the thinner phantom, scattering becomes significant since it creates a loss of contrast even after the G^0 correction.

2.2.1.2 Oxidic melt tests

At present various binary oxidic melt as listed in Table 2.2.1 has been tested to develop the techniques to generate and deliver a single drop melt for the MISTEE experiments. The binary oxide, CaO-B₂O₃, has high viscosity compared to corium and exhibits the characteristics of glass-type oxides. It has relatively low melting point. The other oxides such as Al₂O₃, WO₃-CaO and MnO-TiO₂ have the characteristic of ceramic type of oxides similar to the corium. However, the melting temperatures of these oxides except the WO₃-CaO are much higher. The characteristics of steam explosions, fragmented debris morphology and FCI energetics for those oxidic melt will be tested until the end of the project.

Table 2.2.1 Thermo-physical properties of single and binary oxidic melts for the MISTEE experiments comparing to Corium and Tin

	Corium (80UO ₂ -ZrO ₂)	Sn	Al ₂ O ₃	CaO-B ₂ O ₃ (30-70w/o)	WO ₃ -CaO (82-18w/o)	MnO-TiO ₂ (78-22w/o)
T _{ref} , °C	2600	1000	2800	1100	1200	1400
ρ, kg/m ³	7320 (liq.)	6507	2027	2500 (liq.)	6500 (sol.)	4500
T _{mp} , °C	2600 (liq.) 2500 (sol.)	232	2500	1030 (liq.) 980 (sol.)	1200 (liq.) 1135 (sol.)	1377 (liq.)
C _p , kJ/kgK	0.54 (liq.) 0.41 (sol.)	0.257	1.4	2.20 (liq.) 1.53 (sol.)	0.5	0.9
h _{fus} , kJ/kg	360	59.5	1000	460	70	-
k, W/mK	9.6 (liq.)	32	8	3.0 (liq.) 2.1 (sol.)	-	-
μ, mPa/s	3.7	0.87	4	100~300	-	-
σ, N/m	1.02	0.53	0.5	0.15	-	-

Recently, a MnO-TiO₂ melt at the initial temperature of approximately 1400 °C was successfully delivered into water at 50 °C and visualized with high-speed photography and X-

ray radiography simultaneously. The image in Fig. 2.2.5(a) showed the high temperature melt drop which was deformed during the penetration into water. The Fig. 4.5(b) showed that the droplet has an internal cavity.

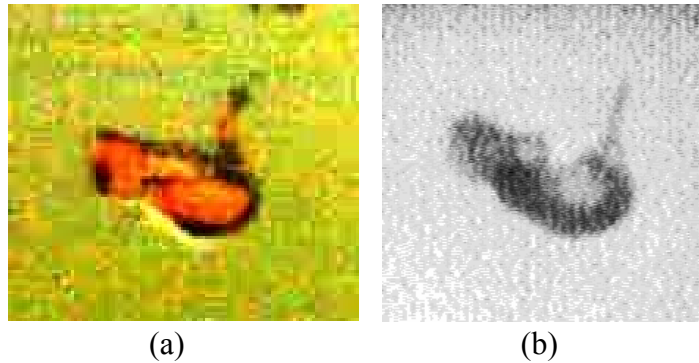


Fig. 2.2.5 MnO-TiO₂ melt drop (~1400 °C) into water: (a) photograph image and (b) X-ray image.

2.2.1.3 Development of simultaneous visualization system

In this year, one significant improvement of our X-ray radiography system in the MISTEE facility has been achieved by adding additional high-speed CMOS camera (Redlake HG50LE Color CMOS Camera, 100,000 fps maximum). This improvement provides the simultaneous synchronized visualization (see Fig. 2.2.6) using two high-speed cameras, one for X-ray radiography and another for photography, called SHARP (Simultaneous High-Speed Acquisition with Radiography and Photography) (see Fig. 2.2.6) where synchronized visual data for vapor bubble and melt fragment dynamics, will enable the accurate quantification of the steam explosions.

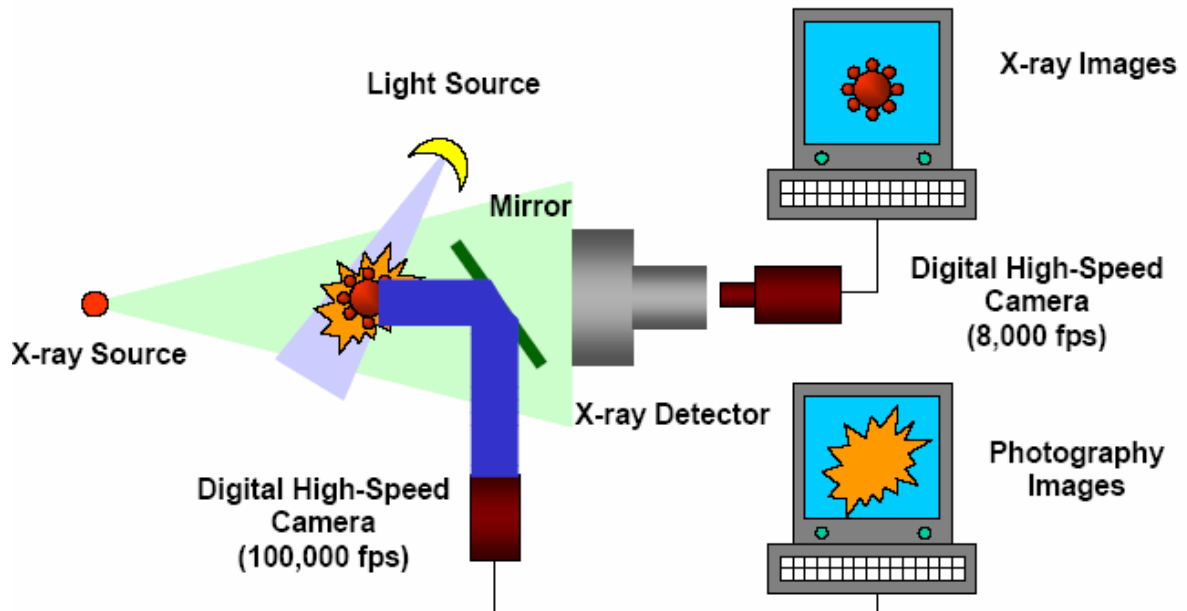


Fig. 2.2.6 The schematic of the SHARP system.

One high-speed camera (photography) visualizes the dynamic behavior of vapor film surrounding a melt drop during the vapor explosion process. This information will provide data on the interaction zone of steam-melt-water mixture as well as the transient steam bubble dynamics. The data on interaction zone will be used to quantify the volume fractions of each component involved in vapor explosion derived from the image data from the X-ray radiography. The data on the transient bubble dynamics in combination with dynamic pressure signals will be used to estimate the energetics or explosivity, of the vapor explosion, in terms of explosion conversion ratio (the ratio of work done by the explosion process on the environment to the total initial energy content of the melt droplet).

The other camera (X-ray radiography) visualizes the melt fragmentation process during the explosion phase of vapor explosion. This image data will provide the visual information on the fine fragmentation and triggering processes and eventually be quantified after a series of calibration tests. This transient fragmentation data will be used to evaluate the current-existing analytical fragmentation models and to propose a new model if necessary. In addition, the X-ray image data will provide the characteristic and location of initial triggering and small-scale propagation processes. Dynamic behavior of finely fragmented melt particles will be also important data to evaluate the existing analytical explosion models which employ local heat transfer among the fine particles, un-fragmented melt, vapor and water in the interaction zone.

Image processing is one of important tasks because the quantification of the fine fragmentation of a melt-drop during the vapor explosion is based on the images taken by both photography and X-ray radiography. In particular, the X-ray images have significant amount of background image noise because of the X-ray back scattering and inefficiency of scintillation detector and phosphor screen. In addition to this, to quantify the data, a series of calibration tests with known geometry and material contents have to be performed.

This system will be the main visualization system to be used in the coming investigation of the MISTEE program.

2.2.2 Steam Explosion Analysis with the COMETA Code

In year 2004, we employed the computer code, COMETA (Core MELt Thermalhydraulic Analysis) developed by JRC (Joint Research Center), at Ispra in Italy, for simulation of the steam explosion phenomena in the L-33 test where an intermediate scale explosion was observed in the facility. Subsequently, the code was applied to investigate the influence of melt fragmentation size and hydrogen concentration on the explosion.

Recently in the TROI test series carried out at KAERI (Korean Atomic Energy Research Institute) in Korea, intermediate scale steam explosions were observed using various conditions of molten corium compositions. The geometry of the TROI set-up, operating conditions and corium compositions and its melt temperature were quite different from that of the FARO L-33 test. It may be noted that the earlier FARO tests with corium did not exhibit any steam explosion except the L-33 test. On the other hand, most of the tests carried out in the TROI facility showed steam explosions. Therefore in order to further understand the explosion phenomena, we simulated the TROI tests using the code. The dynamic pres-

sure for the TROI 13 test was predicted and the pressure profile was compared with the actual tests. Next, we simulated the TROI operating conditions in the FARO L-33 test in order to understand the effects of operating conditions on the dynamic pressure. We retained the mass of melt, hydrogen concentration, drop size and water depth same as that in the L-33 test. But the melt temperature, test section pressure, water subcooling was the same as that in TROI. We found that the melt superheat, subcooling of the water and working pressure play significant roles in causing an explosion. Another important difference between the above two tests was that the depth of water in TROI was much smaller than that in FARO. To study that, we varied the water depth in the FARO geometry for a given operating condition of TROI wherein explosion was observed.

2.2.2.1 Simulation of the FARO L-33 Test

The main objective of the FARO research program was to assess melt-coolant interaction and quenching phenomenology in water-cooled reactors severe accidents. The main components of the test facility includes the furnace, the intersection valve unit, the release vessel, the interaction test section and the venting system. The direct heating UO_2/ZrO_2 granulate compacted between the electrodes generates melt. Then the melt is discharged through an orifice in the center into the release vessel through the release tube. The release vessel is located inside the dome-shaped upper head of the FAT vessel. The FAT test section consists of a vessel of 1.5 m internal diameter and height of about 2 m.

Table 2.2.2. The FARO L-33 test operating conditions

Melt composition	80 % UO_2 + 20 % ZrO_2
Melt mass (kg)	100
Release diameter (m)	0.05
Pressure (MPa)	0.41
Subcooling (K)	124
Water depth (m)	1.62
Melt temperature (K)	3098
Triggering time (s)	1.128

In order to compare the test results with the tests of the previous TERMOS vessel, an internal cylinder of internal diameter of 0.71 m is inserted. Only this cylinder is filled with water and the outer annulus space is part of free volume. A debris catcher is mounted in the lower part of the internal vessel. The volume occupied by the water above the debris catcher is 0.628 m³ and the corresponding free surface is 1.62 m. A detailed description of the facility is given in the reference and Table 2.2.2 shows the operating conditions of the FARO L-33 Test.

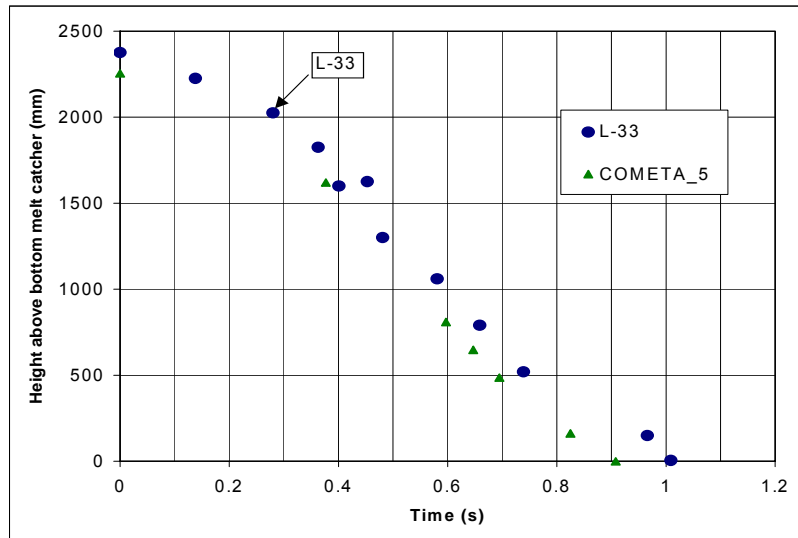


Fig. 2.2.7 Simulation of melt jet trajectory using the COMETA

One of the important parameters which could play a role in the steam explosion is the amount of hydrogen produced in the L-33 test. Subsequent to the tests, it was estimated that about 29.8 g of hydrogen could have been produced. However, this value depends on the mass of the fragmented melt mass which was unknown. Hence, in the simulation this value was varied in order to understand its effect on the steam explosion behavior.

Fig. 2.2.7 shows the melt jet leading edge trajectory as predicted by the COMETA code and its comparison with the L-33 data. The jet reaches the bottom of the test section, i.e. in the catcher at around 1 s as seen both by experiment and predictions. The prediction shows it to be little earlier.

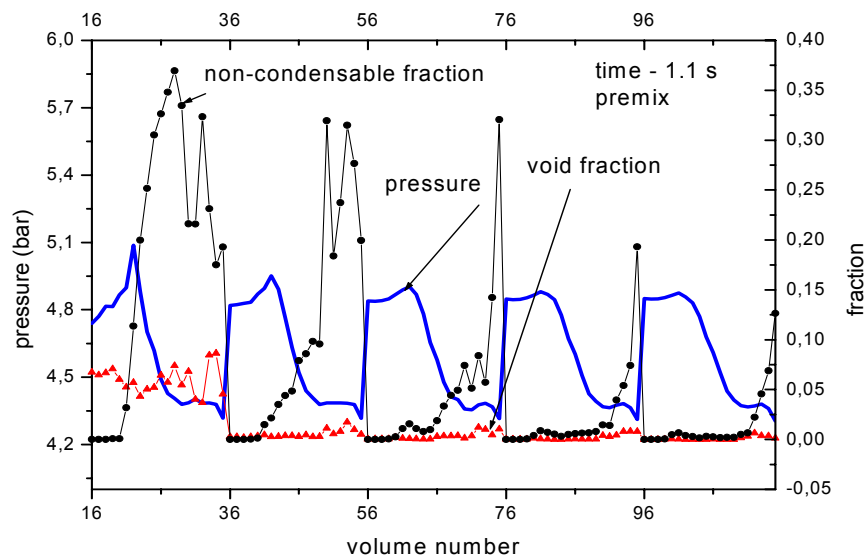


Fig. 2.2.8 Thermal hydraulic behavior during the premix phase at 1.1 s in FARO L-33 test.

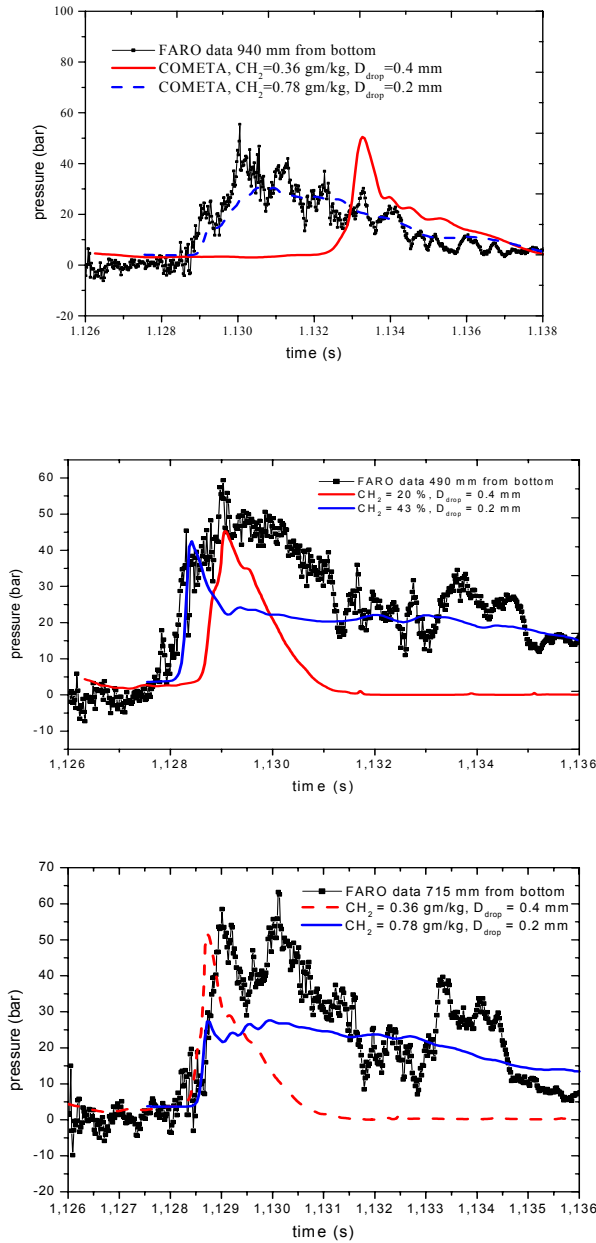


Fig. 2.2.9 Comparison of COMETA prediction with FARO data at 490, 715 and 940 mm from bottom of test section (from the top plot).

The thermal hydraulic phenomena during melt-water interaction at 1.1s is shown in Fig. 2.2.8. As expected, water vaporizes in the volumes 16 to 35 wherein the melt flows. The void fraction is almost zero elsewhere in the water pool. The non-condensable void fraction is higher at the central volume wherein the melt-water interaction takes place. The non-condensable gases are carried to the surrounding regions by diffusion. The pressure is almost constant throughout the water pool. This is slightly higher at the central location due to presence of larger non-condensable gas and steam.

It is reported that two of the most important parameters which can influence the pressure spike during the melt water interactions, are the hydrogen production and the drop sizes during fragmentation of the melt. Both these parameters are too difficult to predict accurately. In fact, the sizes of the drop formed during fragmentation can vary from a lower limit to an upper limit. In the simulation, an average size of the drop was considered.

Fig. 2.2.9 shows the comparison of the pressure transient at different positions on the vessel wall after trigger was activated at the bottom of the pool (volume 16). In all these cases, two different hydrogen concentrations were considered, i.e. 0.78 gram of hydrogen per kg of melt and 0.36 gram per kg of fragmented melt. Similarly, two different drop sizes were considered, i.e. drop size of 0.2 mm and 0.4 mm. These values were chosen in order to understand their influence on the pressure spike. From these results it is clear that a small value of hydrogen concentration and drop size gives a larger value of pressure spike. However, the hydrogen concentration of 43 % and drop size of 0.2 mm shows closer agreement to the measured value at the lower as well as at the upper parts of the vessel.

Table 2.2.3 The TROI-13 test operating conditions

Melt composition	70 % UO ₂ + 30 % ZrO ₂
Melt mass (kg)	7.7
Release diameter (m)	0.056
Pressure (MPa)	0.1
Subcooling (K)	81
Water depth (m)	0.67
Melt temperature (K)	3500
Triggering time (s)	Exactly not known

2.2.2.2 Simulation of TROI experiments

The configuration is similar to that of FARO facility. However, the melt compositions, facility dimensions and operating conditions were different from the FARO facility. In most of the FARO tests, the UO₂/ZrO₂ ratio was 70/30 unlike in FARO wherein it was 80/20. The operating pressure in TROI was near atmospheric which was much lower than the FARO (about 4 bar). The water subcooling was much lower in TROI than that in FARO. While the test section diameter in both facilities were of the same order, the depth of water pool in FARO was 1.62 m and that in TROI it was only 0.67 m. These variations could bring significant changes in the dynamic pressure behavior in both facilities following the trigger. In this work, we have simulated the TROI 13 test explosion behavior using the code COMETA for which the dynamic pressure profile is available. Table 2.2.3 shows the main operating conditions for the test. It may be noted that this test had the problem of correct measurement of the melt temperature and the premix time phase is not exactly known. The amount of hydrogen generated in TROI 13 test has been reported to be less than 1 gram, which is much smaller than that of the FARO L-33 test. In the code, we used 0.001 gm per kg of melt, which is almost negligible.

Before analyzing the dynamic pressure behavior after trigger is actuated, it is essential to know the thermal hydraulic behavior during the premix phase. The dynamic pressure behavior during the premix period is shown in Fig. 2.2.10. It may be noted that at about 0.95 s, the pressure starts oscillating when the melt interacts with the water during its passage resulting void formation. This implies that the mixture was almost ready to explode had there been an external trigger at this time.

The peak pressure measured in TROI 13 was about 7 MPa. The duration of the highest peak was about 1 ms and it took 1.22 s for the occurrence of energetic steam explosion after the actuation of puncher. In the predictions, we have varied the drop diameter like the previous case. For smaller drop diameter, the predicted and measured peak pressure spike is closer; however with increase in drop diameter, the peak pressure on the wall reduces

As said before, the TROI operating conditions were much different from FARO. The melt temperature was much higher than that in FARO and the operating pressure was atmospheric in TROI while the operating pressure was about 4 bars in FARO. The peak pressure spike in TROI-13 was much higher than that observed in FARO L-33 test. In order to understand how the operating conditions influence the explosion behavior, we have simulated the operating conditions of TROI in FARO geometry. In this work, we have varied the melt superheat and water depth and their effects on the explosion behavior have been investigated.

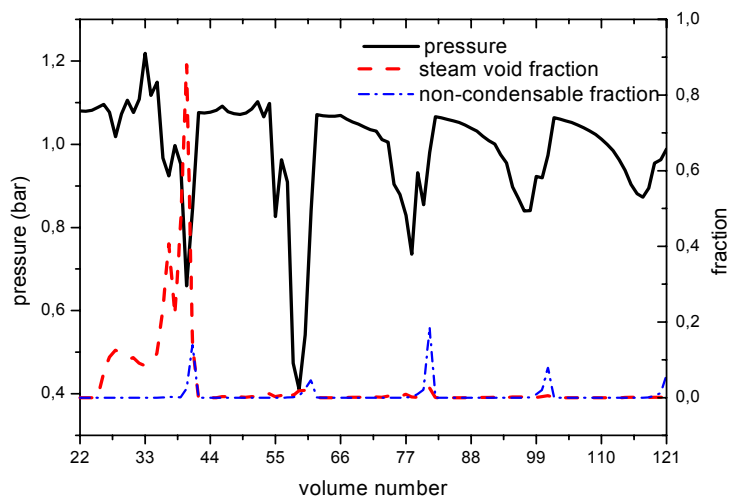


Fig. 2.2.10 Thermal hydraulic phenomena during premix phase in TROI-13 at 0.95

Fig. 2.2.11 shows the dynamic pressure profile at the bottom of the FARO test section wall for the melt temperature of 3800 K keeping the hydrogen concentration of 43 % (same as that in FARO). The melt temperature in TROI-12 was 3800 K and that in TROI-13 was more than 3500 K. So we kept the melt temperature in this case at 3800 K. The operating pressure was kept at 1 bar similar to that of TROI case. It is interesting to note that a second pressure spike is observed at about 1.133 s which is not observed for the corresponding case in FARO. The peak pressures were slightly lower than the corresponding case in FARO due to higher void formation under low pressure conditions. Reduction

of melt temperature to 3000 K as that in TROI-14 does not show any pressure spike. This implies that a larger melt superheat causes a larger pressure spike. However, with the same conditions reduction of hydrogen concentration can cause a stronger pressure spike. Another difference between the TROI and FARO operating conditions was the depth of water pool as said before. To understand the influence of water depth on dynamic pressure profile, we varied the water pool depth from 1.2 m to 2m in FARO. The results indicate that the pressure spike is a maximum at about 1.6 m when the melt is able to reach the bottom of the pool and the fragmentation is complete to cause a spontaneous explosion.

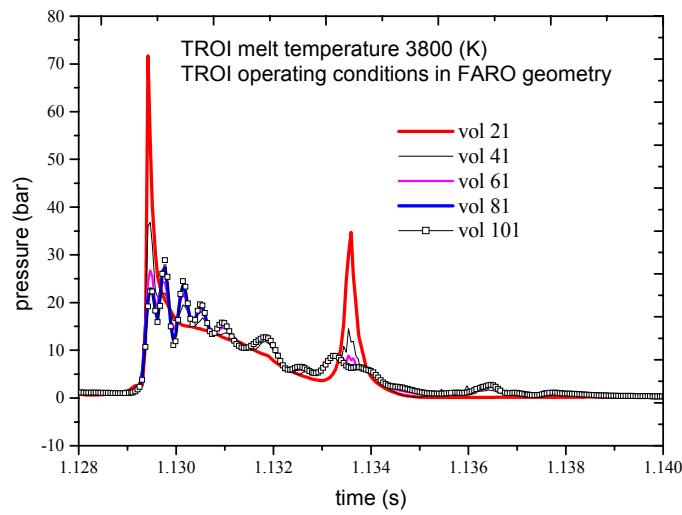


Fig. 2.2.11 Effect of TROI operating conditions in FARO geometry on the dynamic pressure profile

3 SUMMARY OF YEAR 2004 RESEARCH PROGRAM

The summary of the year 2004 research activities are described below.

In-Vessel and Ex-Vessel Debris Bed Coolability

In the year 2004, we have investigated experimentally the quenching behavior of a simulated radially stratified heat generating porous debris bed, which can be formed in an unlikely severe accident in a nuclear reactor. To simulate the non-condensable gases generated during an MCCI, which can affect the flooding and quenching behavior, air and argon at different flow rates were injected at the bottom of the bed. The quenching behavior under top and bottom flooding conditions were studied in order to find an effective means of quenching of the bed, and generation of data for model development and code validation. The following main observations resulted from this study:

- The quenching rate with top flooding alone is very small and with non-condensable gases during MCCI, CCFL conditions may exist and it may not be possible to quench the bed.
- Water injection at the periphery of the bed reduces the quenching period. However, bottom flooding using downcomers in addition to top flooding reduces the quenching period significantly. The quenching period is found to be affected by the location and size of the downcomers which bring water from the top overlayer water to the bottom of the bed.
- Quenching rate in the low porosity layer is always found to be lower than that in the high porosity layer.
- Non-condensable gases systematically delay the quenching rate both in low and high porosity layers. However, this effect was found to be larger in the higher porosity layer than in the lower porosity layer.
- The quenching behavior was almost similar with air and argon. However, the quenching period was found to be little longer with argon than with air for the same injection mass flow rate.

In-Vessel and Ex-Vessel Melt Coolability (COMECO Program)

In the year 2004, experiments were carried out with the melt prepared from the binary oxide mixture of CaO (30% by wt.) and B₂O₃ (70% by wt.) and MnO+TiO₂ melt. The preliminary results confirmed the general quenching behavior of melt due to the top flooding. The post-test observation showed the structure of the quenched melt. A number of attempts with MnO+TiO₂ melt were failed due to the high temperature of the melting point of the mixture and it is difficult to achieve with the existing furnace. The COMECO

melt generation system was under repair. It is expected that some delay on the COMECO experiments for ex-vessel coolability of molten pool will occur due to the failure of the induction melt generator system.

Melt Pool Convection (SIMECO Program)

Experimental investigations were conducted in two and three-layer stratified pool in a scaled vessel of a prototype PWR, which can happen during a low probability severe accident. The results are useful for understanding the convection heat transfer characteristics inside the stratified pool and determination of the thermal load in the reactor vessel. The following are the main conclusions obtained from this study.

- The interfacial resistance between the stratified heated layers can reduce the upward convective heat transfer significantly. However, this resistance was found to be larger in case of a two-layer pool as compared to that in case of a three-layer pool.
- The heat flux distribution in the vessel wall is found to be similar in case of two-layer and three-layer pools. However, the location of peak heat flux shifts upward in case of a three-layer pool.
- Presence of chlorobenzene in the lower layer of the three-layer pool is found to augment the heat transfer in the lower part of vessel and hence reduces the thermal load on the lower part of the vessel.
- In all the cases, the interfacial resistance between the stratified heated layers was found to reduce the upward convective heat transfer rate. However, this resistance was found to be the strongest when the top layer remained unheated and only middle and partly lower layer were generating heat.
- The upward to downward heat flux ratio is found to be around 0.3 and has a small variation with Rayleigh number or difference in heating conditions in the pool and did not change substantially from that for the two-layer pool.

Steam Explosion Loads (MISTEE Program)

It is clear that the existing experiments, so far, indicate that the conversion ratio (or energetic yield) in a triggered $\text{UO}_2\text{-ZrO}_2$ explosion is significantly less than that in a triggered Al_2O_3 or stainless steel melt explosion. There are some limiting mechanisms which reduce the yield for non-eutectic oxidic mixtures. In this context we still have to establish if the $\text{UO}_2\text{-ZrO}_2\text{-Zr}$ mixture will behave differently from the $\text{UO}_2\text{-ZrO}_2$ mixture.

Since it is infeasible to perform large-scale steam explosion experiments with $\text{UO}_2\text{-ZrO}_2$ or $\text{UO}_2\text{-ZrO}_2\text{-Zr}$ and it is very difficult to establish a scaling relationship, we believe that a more fundamental investigation will bear fruit in terms of identifying the limiting mechanisms. We accomplished this for the jet break-up phenomenon and now we have constructed the micro interaction steam explosion experiments (MISTEE) facility, wherein, currently, we are observing the differences between the character of the explosion phase of a steam explosion, for a single droplet, of different material (metal, single oxide, binary oxide mixture, binary oxide and metal mixture, etc.) melts. We obtain con-

version ratio by employing a very fast pressure transducer. As experimental parameters, we vary the subcooling of water, trigger strength and the melt droplet superheat.

The collected data are synthesized to identify the possible limiting mechanisms (key thermo-physical properties) in the oxidic melts. This will suggest the reason why the metallic and some oxidic melts have higher triggerability and explosivity in comparison with others, which have much lower triggerability and explosivity. The assessment analysis based on a statistical design model will be performed to identify the key parameters including thermo-physical properties, which affect the triggerability and explosivity of vapor explosion. In addition, our analytical model for the triggerability and explosivity will be developed by considering the data collected in this project and the improved model will be used for the scaling analysis needed to evaluate the explosivity of prototypic melt in prototypic accident conditions. The mechanisms that limit the triggerability and explosivity of $\text{UO}_2\text{-ZrO}_2$ will be identified.

In this year, the followings are the summary of the activities in the MISTEE facility;

- Completions of the metallic melt tests with molten tin droplet.
- Evaluation of quantification methodology of X-ray radiography.
- Development of simultaneous synchronized X-ray radiography and photography system.
- Development of oxidic melt generation and delivery system

Steam Explosion Loads (COMETA Analysis)

The COMETA code was originally developed for simulation of FARO melt-water interaction experiments. Almost all previous FARO experiments except that of the L-33 test did not show any explosion and the FARO code had simulated the quenching behavior quite successfully. In this work, we have further tested the capability of the COMETA code for the explosion behavior observed in L-33 test. Then we verified the code with the steam explosion behavior observed in the TROI 13 test. Even though the TROI geometry was similar, but the dimensions and operating conditions were quite different from FARO L-33 test. The TROI 13 test had yielded a larger pressure spike as compared to that in the FARO L-33 test. To understand the influence of operating conditions on the pressure spike, we simulated the TROI operating conditions in FARO geometry. The main parameters that were varied are the melt super heat and water depth. The main conclusions obtained from this study are

- The code is able to simulate the melt-water interaction with certain values of non-condensable gas concentration and drop size.
- The dynamic pressure spike is stronger with smaller hydrogen concentration and fragmented drop size. Similar behavior was also observed with larger melt superheat.
- There is an optimum water depth at which the pressure is maximum during melt water interactions.

4 RESEARCH PLAN OF YEAR 2005 RESEARCH PROGRAM

During the year 2005, activity in the MSWI project is focused toward two major issues threaten the integrity of Swedish BWR plant, namely ex-vessel steam explosion and melt coolability. Experimental and analytical works for the MISTEE program will continue to understand the fundamental physics behind the complex steam explosion process and energetics of FCIs. In-depth analysis of the coolability in particulated debris bed and melt pool will be performed.

Reference (2004 Publication List)

Published or in Process of Publication

1. Sehgal, B. R. and Park, H. S., "Final Report on PRE-DELI-MELT. Pre-Project (PRE) on Development and Validation (DELI) of Melt Behavior (MELT) in Severe Accidents," **NKS-99**, ISBN 87-7893-158-4, (2004).
2. Sehgal, B. R., "Is it the End of History for LWR Safety?" Keynote paper in the 6th International Topical Meeting on Operating Nuclear Reactor Thermal Hydraulics, Operations and Safety (NUTHOS6), Nara-Ken, New Public Hall, Nara, Japan.
3. Sehgal, B. R., "Stabilization and Termination of Severe Accidents in LWR," **Nucl. Eng. and Des.**, 2005.
4. Sehgal, B. R., Giri, A., Chikkanagoudar, U., Karbojian, A., "Experiments on In-Vessel Melt Coolability in the EC-FOREVER Program," **Nucl. Eng. and Des.**, 2005.
5. Sehgal, B. R., Karbojian, A., Giri, A., Kymäläinen, O., Bonnet, J. M., Ikonen, K., Sairanen, R., Bhandari, S., Buerger, M., Dienstbier, J., Techy, Z., Theofanous, T., "Assessment of Reactor Vessel Integrity (ARVI)," **Nucl. Eng. and Des.**, 2004.
6. Sehgal B. R., Stepanyan A., Nayak A. K., Chikkanagoudar, U., "Natural Convection Heat Transfer in a Stratified Pool with Volumetric Heat Generation," Proc. of the 6th Inter. Top. Meeting on Operating Nuclear Reactor Thermal Hydraulics; Nara, Japan, Oct. 4-8, 2004
7. Jasiulevicius, A., Konovalikhin, M. J., Sehgal, B.R., "Investigations on Enhancement of Corium Coolability with CRGTs in the Lower Head of a BWR," **Nucl. Eng. and Des.**, 2005.
8. Nayak, A. K., Stepanyan, A., and Sehgal B. R., "Quenching behaviour of a volumetrically heated particulate bed with non-condensable gases addition from bottom", the 42nd European two-phase flow group meeting, Genova, Italy, June 2004.
9. Park, H. S., Hansson, R. C., and Sehgal, B. R., "Fine Fragmentation of Molten Droplet in Highly Subcooled Water Due to Vapor Explosion Observed by X-ray Radiography," On-line print in **J. of Exp. Therm. and Fluid Sci.**, (2004).
10. Giri, A., Park, H. S., and Sehgal, B. R., "Analysis of Bubble Dynamics in Explosive Boiling of Droplet with Fine Fragmentation," On-line print in **J. of Exp. Therm. and Fluid Sci.**, (2004).
11. Hansson, R. C., Park, H. S., and Sehgal, B. R., "Evaluation of Quantitative Measurement by High-speed X-ray Radiography for Fragmented Particle Fraction," Proc. of the 6th International Topical Meeting on Nuclear Reactor Thermal Hydraulics, Operations and Safety, NUTHOS6-000317, October 4 - 8, 2004, Nara-Ken, New Public Hall, Nara, Japan.

12. Nayak, A. K., Park, H. S., Annunziato, A. and Sehgal, B. R., "Investigations on Steam Explosion Phenomena with FARO and TROI Experiments," Proc. of the 6th International Conference on Simulation Methods in Nuclear Engineering, Montreal, Quebec, Canada, October 13~15, 2004.
13. Park, H. S., Shiferaw, D., Sehgal, B. R., Kim, D. K., and Mamoun, M. "Film Boiling Heat Transfer on a High Temperature Sphere in Nanofluid," 2004 ASME Heat Transfer/Fluids Engineering Summer Conference, HT-FED2004-56471, Westin Charlotte & Convention Center Charlotte, North Carolina, USA, July 11-15, 2004.
14. Stepanyan, A., Nayak A. K., and Sehgal B. R., "Experimental Investigations of Natural Convection in a Three Layer Stratified Pool with Internal Heat Generation", Proc. of the International Topical Meeting on Operating Nuclear Facility Safety; Washington, USA, Nov. 14-18, 2004

In Preparation

15. Hansson R. C., Park, H. S., and Sehgal, B. R., "Single Drop Steam Explosions of Binary Oxides in Subcooled Water," submitted to the 11th International Topical Meeting on Nuclear Reactor Thermal-Hydraulics (NURETH-11), Log Number: 463, Popes Palace Conference Center, Avignon, France, October 2-6, 2005.
16. Ma, W., Aram K., and Sehgal, B. R., "Experiments on Natural Circulation of Lead-Bismuth in the TALL Test Facility," submitted to the 11th International Topical Meeting on Nuclear Reactor Thermal-Hydraulics (NURETH-11), Log Number: 277, Popes Palace Conference Center, Avignon, France, October 2-6, 2005.
17. Nayak, A. K., Stepanyan, A., and Sehgal, B.R., "Investigations on the dryout behavior of a radially stratified porous bed", submitted to the 11th International Topical Meeting on Nuclear Reactor Thermal-Hydraulics (NURETH-11), Log Number: 313, Popes Palace Conference Center, Avignon, France, October 2-6, 2005.
18. Nayak, A. K., Park, H. S., Annunziato, A. and Sehgal, B. R., "Simulation of TRIO Steam Explosion Behaviour Using the COMETA Code," submitted to the 11th International Topical Meeting on Nuclear Reactor Thermal-Hydraulics (NURETH-11), Log Number: 185, Popes Palace Conference Center, Avignon, France, October 2-6, 2005.
19. Nayak, A. K., Stepanyan, A., and Sehgal, B.R., "An experimental simulation study of debris quenching in a radially stratified porous bed", submitted to the 11th International Topical Meeting on Nuclear Reactor Thermal-Hydraulics (NURETH-11), Log Number: 314, Popes Palace Conference Center, Avignon, France, October 2-6, 2005.
20. Nayak, A. K., Stepanyan, A., and Sehgal, B.R., "Quenching behavior of a radially-stratified particulate bed with non-condensable gases addition from bottom", submitted to the 2005 International Congress on Advances in Nuclear Power Plants (ICAPP-05), Seoul, Korea, 2005.
21. Sehgal, B. R., Nayak, A. K., and Srinivas Rao, R., "Study on Water Ingression Phenomena in Melt Pool Coolability", submitted to the 11th International Topical Meeting on Nuclear Reactor Thermal-Hydraulics (NURETH-11), Log Number: 449, Popes Palace Conference Center, Avignon, France, October 2-6, 2005.
22. Stepanyan, A., Nayak, A. K., and Sehgal, B. R., "Natural Convection in a Three-Layer Stratified System with Internal Heat Generation, under Isothermal and Adiabatic Boundary Conditions," submitted to the 11th International Topical Meeting on Nuclear Reactors Thermal-Hydraulics (NURETH-11), Log Number: 312, Avignon, France, October 2-6, 2005

www.ski.se

STATENS KÄRNKRAFTINSPEKTION
Swedish Nuclear Power Inspectorate

POST/POSTAL ADDRESS SE-106 58 Stockholm

BESÖK/OFFICE Klarabergsviadukten 90

TELEFON/TELEPHONE +46 (0)8 698 84 00

TELEFAX +46 (0)8 661 90 86

E-POST/E-MAIL ski@ski.se

WEBBPLATS/WEB SITE www.ski.se